

1 **Ocean bottom distributed acoustic sensing for oceanic seismicity detection and**  
2 **seismic ocean thermometry**

3 **Zhichao Shen<sup>1</sup> and Wenbo Wu<sup>1</sup>**

4 <sup>1</sup>Department of Geology and Geophysics, Woods Hole Oceanographic Institution, Woods Hole,  
5 MA, USA

6 Corresponding author: Zhichao Shen ([zhichao.shen@whoi.edu](mailto:zhichao.shen@whoi.edu))

7 **Key Points:**

- 8       • We develop a curvelet denoising scheme for ocean bottom distributed acoustic sensing to  
9       enhance *T*-wave signals.
- 10       • The denoised distributed acoustic sensing data detects three times more *T*-wave events than  
11       cabled ocean bottom seismometers.
- 12       • The improved detection capability makes more small repeating earthquakes usable for  
13       seismic ocean thermometry.

**14 Abstract**

15 A *T*-wave is a seismo-acoustic wave that can travel a long distance in the ocean with little  
16 attenuation, making it valuable for monitoring remote tectonic activity and changes in ocean  
17 temperature using seismic ocean thermometry (SOT). However, current high-quality *T*-wave  
18 stations are sparsely distributed, limiting the detectability of oceanic seismicity and the spatial  
19 resolution of global SOT. The use of ocean bottom distributed acoustic sensing (OBDAS), through  
20 the conversion of telecommunication cables into dense seismic arrays, is a cost-effective and  
21 scalable means to complement existing seismic stations. Here, we systematically investigate the  
22 performance of OBDAS for oceanic seismicity detection and SOT using a 4-day Ocean  
23 Observatories Initiative community experiment offshore Oregon. We first present *T*-wave  
24 observations from distant and regional earthquakes and develop a curvelet denoising scheme to  
25 enhance *T*-wave signals on OBDAS. After denoising, we show that OBDAS can detect and locate  
26 more and smaller *T*-wave events than regional OBS network. During the 4-day experiment, we  
27 detect 92 oceanic earthquakes, most of which are missing from existing catalogs. Leveraging the  
28 sensor density and cable directionality, we demonstrate the feasibility of source azimuth estimation  
29 for regional Blanco earthquakes. We also evaluate the SOT performance of OBDAS using pseudo-  
30 repeating earthquake *T*-waves. Our results show that OBDAS can utilize repeating earthquakes as  
31 small as M3.5 for SOT, outperforming ocean bottom seismometers. However, ocean ambient  
32 natural and instrumental noise strongly affects the performance of OBDAS for oceanic seismicity  
33 detection and SOT, requiring further investigation.

**34 Plain Language Summary**

35 Oceanic earthquakes can produce loud sounds in the ocean. These sounds usually arrive at a  
36 seismic station as the tertiary wave, a so-called *T*-wave, following the arrival of the primary *P*-  
37 wave and secondary *S*-wave. *T*-waves can propagate thousands of kilometers in the ocean's  
38 SOFAR (SOund Fixing And Ranging) channel with little energy loss. Thus, they are useful for  
39 monitoring earthquakes and ocean temperature changes. However, currently available instruments  
40 for measuring these waves are limited. Recently, a new type of technique, Distributed Acoustic  
41 Sensing (DAS), provides an opportunity to expand the seismic-recording capability in the ocean.  
42 Ocean bottom distributed acoustic sensing (OBDAS) can effectively turn submarine  
43 telecommunication cables into dense seismic sensors that complement conventional seismometers.  
44 In this study, we explore the OBDAS potential for *T*-wave detection. With a 4-day OBDAS  
45 community experiment offshore Oregon, we demonstrate that OBDAS does a better job than a  
46 conventional seismic network for detecting *T*-waves when a specifically designed denoising  
47 scheme is applied. In addition, OBDAS has the potential to measure ocean temperature changes  
48 using more repeating earthquakes of smaller magnitudes, outperforming conventional sensors.  
49 However, the accuracy of the OBDAS system can be strongly affected by various types of noise,  
50 which requires further research.

## 51 **1 Introduction**

52 As a tertiary arrival after the *P*-wave and *S*-wave on seismograms, the seismo-acoustic *T*-wave  
53 propagates horizontally at a speed of  $\sim 1.5$  km/s along the ocean SOund Fixing And Ranging  
54 (SOFAR) channel, where ocean sound speed reaches a minimum (Tolstoy & Ewing, 1950;  
55 Linehan, 1940). Generated from earthquakes and a number of acoustic sources in the water column,  
56 *T*-waves can travel a long distance ( $>1000$  km) with little energy loss. *T*-waves exhibit spindle-  
57 shaped, high-frequency ( $>1$  Hz) waveforms on hydrophones (Fox et al, 1995), ocean bottom  
58 seismometers (OBS; Hamada, 1985), autonomous MERMAID floats (Simon et al., 2021), and  
59 even land stations (e.g., Buehler & Shearer, 2015). Since their early documentations in the 1930s  
60 (Jagger, 1930; Collins, 1936), *T*-waves have been widely used to monitor oceanic seismicity (Fox  
61 et al., 2001; Smith et al., 2002; Dziak et al, 2004; Hanson & Bowman, 2006; Parnell-Turner et al.,  
62 2022) and volcanism (Wech et al, 2018; Tepp & Dziak, 2021), promote tsunami warning (Okal &  
63 Talandier, 1986; Matsumoto et al., 2016), determine earthquake properties (Walker et al., 1992;  
64 de Groot-Hedlin, 2005), discriminate explosive and seismic sources (Talandier & Okal, 2001,  
65 2016), infer detached slabs (Okal, 2001), and constrain crustal attenuation (Koyanagi et al., 1995;  
66 Zhou et al., 2021), significantly broadening our understanding of tectonic process in the remote  
67 ocean (Dziak et al., 2012) and seismo-acoustic wave genesis and propagation (Okal, 2008).

68 *T*-waves can also provide valuable insights to long-term deep ocean temperature changes. With  
69 more than 90% of excess heat due to the greenhouse effect being absorbed, the ocean is  
70 experiencing a secular warming trend of  $\sim 0.02$  K per decade (Wunsch, 2016). Since the ocean is  
71 an efficient hydroacoustic transmitter and sound speed in seawater increases with temperature, Wu  
72 et al. (2021) developed seismic ocean thermometry (SOT) to quantify basin-scale ocean  
73 temperature changes from the travel time changes of *T*-waves generated by repeating earthquakes.  
74 This idea was inspired by the ocean acoustic tomography proposed by Munk and Wunsch (1979).  
75 While the latter concept, which utilizes active sources, has achieved great success (Munk et al.,  
76 1994; ATOC Consortium, 1998), the cost-efficient SOT approach has shown great potential to  
77 complement modern Argo Climatology data (Riser et al., 2016) in a passive way. Applying SOT  
78 to the equatorial Indian Ocean revealed ocean dynamic signals at various time scales and depths  
79 including seasonal changes, meso-scale eddies and equatorial waves (Wu et al., 2021; Callies et  
80 al., 2023), that demonstrates its potential to complement existing ocean temperature observations.

81 A further expansion of oceanic seismicity monitoring and SOT to the global ocean requires the  
82 establishment of long-term stations to record high-quality *T*-waves. However, suitable *T*-wave  
83 stations remain sparsely distributed, the Comprehensive Nuclear-Test-Ban Treaty Organization  
84 (CBTBO) operating a handful of hydrophone stations (Figure 1a), and with other networks  
85 maintaining a few island stations and a limited number of offshore cabled sites, greatly limiting  
86 the spatial coverage of oceanic seismicity monitoring and global SOT. In particular, the coverage  
87 of the Arctic and Southern Oceans (Figure 1a) is extremely poor, highlighting an urgent need for  
88 more observations to fill the gap. Meanwhile, deploying and maintaining long-term, high-quality

89 *T*-wave instrumentation in the harsh ocean environment is a significant logistical and financial  
90 challenge.

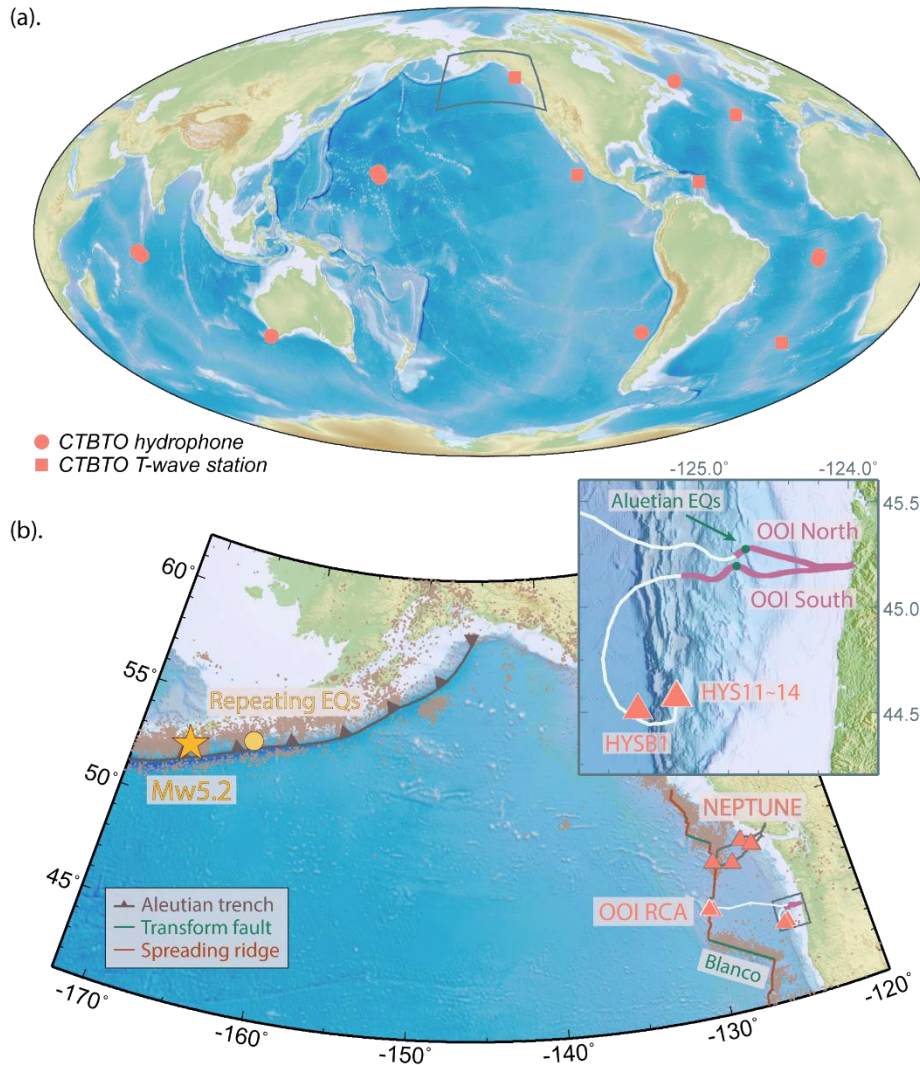
91 Distributed acoustic sensing (DAS) is a new and promising technology that offers a cost-efficient  
92 and scalable solution for deploying large-aperture, long-term, dense seismic arrays. By converting  
93 Rayleigh-type backscattering due to intrinsic fiber impurities to longitudinal strain or strain rate,  
94 DAS repurposes pre-existing telecommunication fiber-optic cables into arrays of thousands of  
95 vibration sensors (Hartog, 2017). With up to ~100 km aperture and sensor spacing of a few meters,  
96 DAS can record high frequency wavefields at unprecedented spatiotemporal resolution, making it  
97 a compelling tool for a range of geophysical settings (Zhan, 2020; Lindsey & Martin, 2021). In  
98 underwater environments, ocean bottom DAS (OBDAS) has been successfully used as a very  
99 broadband instrument (Ide et al., 2021) to detect earthquakes (Lior et al., 2021), illuminate seafloor  
100 faults (Lindsey et al., 2019), characterize marine sediment (Spica et al., 2020; Cheng et al., 2021;  
101 Viens et al., 2022), monitor ocean dynamics (Sladen et al., 2019; Williams et al., 2019, 2022) and  
102 map offshore wind turbines (Williams et al., 2021). With air-gun shots, Matsumoto et al., (2021)  
103 demonstrated that OBDAS is effective in sensing hydroacoustic signals across a broad frequency  
104 range from a tenth to a few tens of Hz. Recently, Ugalde et al., (2022) presented *T*-wave  
105 observations on OBDAS in the Canary Islands from several regional and distant earthquakes.  
106 However, due to limited observations, the performance of OBDAS for oceanic seismicity detection  
107 and SOT has not yet been systematically investigated.

108 In this study, we use data from a 4-day community experiment conducted offshore central Oregon  
109 to examine *T*-waves on OBDAS. To identify potential *T*-wave candidates on OBDAS, we first  
110 build a *T*-wave catalog using Ocean Networks Canada cabled OBS and hydrophone array. With  
111 this catalog, we identify *T*-wave observations on OBDAS and develop a curvelet denoising  
112 algorithm to enhance *T*-wave signal-to-noise ratios. The application of curvelet denoising on  
113 OBDAS enables us to detect 92 *T*-wave events, three times the number identified in the NEPTUNE  
114 *T*-wave catalog. Meanwhile, the OBDAS cable directionality enables us to constrain the source  
115 azimuth of regional Blanco earthquakes through array beamforming. With the enhanced detection  
116 capability, we propose a new workflow for SOT with OBDAS by taking advantage of a larger  
117 number of usable small repeating earthquakes compared to the OBS data. Lastly, we also discuss  
118 the noise in OBDAS data, which requires further investigation.

## 119 **2 Data**

120 The Ocean Observatory Initiative (OOI) Regional Cable Array (RCA) offshore central Oregon is  
121 a long-term infrastructure designed to facilitate integrated investigations into both volcanic and  
122 coastal systems (Kelly et al., 2014). It provides real-time telemetry for over 140 instruments,  
123 including OBSs, remote access fluid samplers, DNA samplers, acoustic doppler current profilers  
124 and so on. The OOI RCA observatory is powered by and communicates through two  
125 telecommunication fiber-optic subsea backbone cables, with the northern branch extending to

126 Axial Seamount and the southern branch running to the Oregon shelf (Figure 1b). Since 2015, five  
 127 OBSs have been deployed near Southern hydrate ridge (Figure 1b) in order to monitor oceanic  
 128 seismicity, track melt migration, and whale vocalizations, with four located at the ridge summit at  
 129 a water depth of ~800 m (HYS11-14) and one situated at the slope base at a water depth of ~2900  
 130 m (HYSB1).



131  
 132 **Figure 1.** The CTBTO hydrophone network and our study region. (a). Global CTBTO  
 133 hydrophones and *T*-wave stations. The gray box illustrates our study region. (b). Map view of our  
 134 study region with background tectonics and seismicity, cabled ocean observatories (ONC  
 135 NEPTUNE and OOI RCA; orange triangles), and OOI OBDAS. The insert panel (top right) is a  
 136 zoom-in view of OBDAS (purple lines) and OBSs at OOI. The green dots indicate the locations  
 137 where the OOI North and South cables turn southward. White lines denote entire backbone cables.  
 138 The green arrow represents the *T*-wave propagation direction from Aleutian earthquakes.

139 During a scheduled maintenance period of the OOI RCA platform in November 2021, a four-day  
 140 community experiment was conducted to explore the potential of submarine DAS for observing

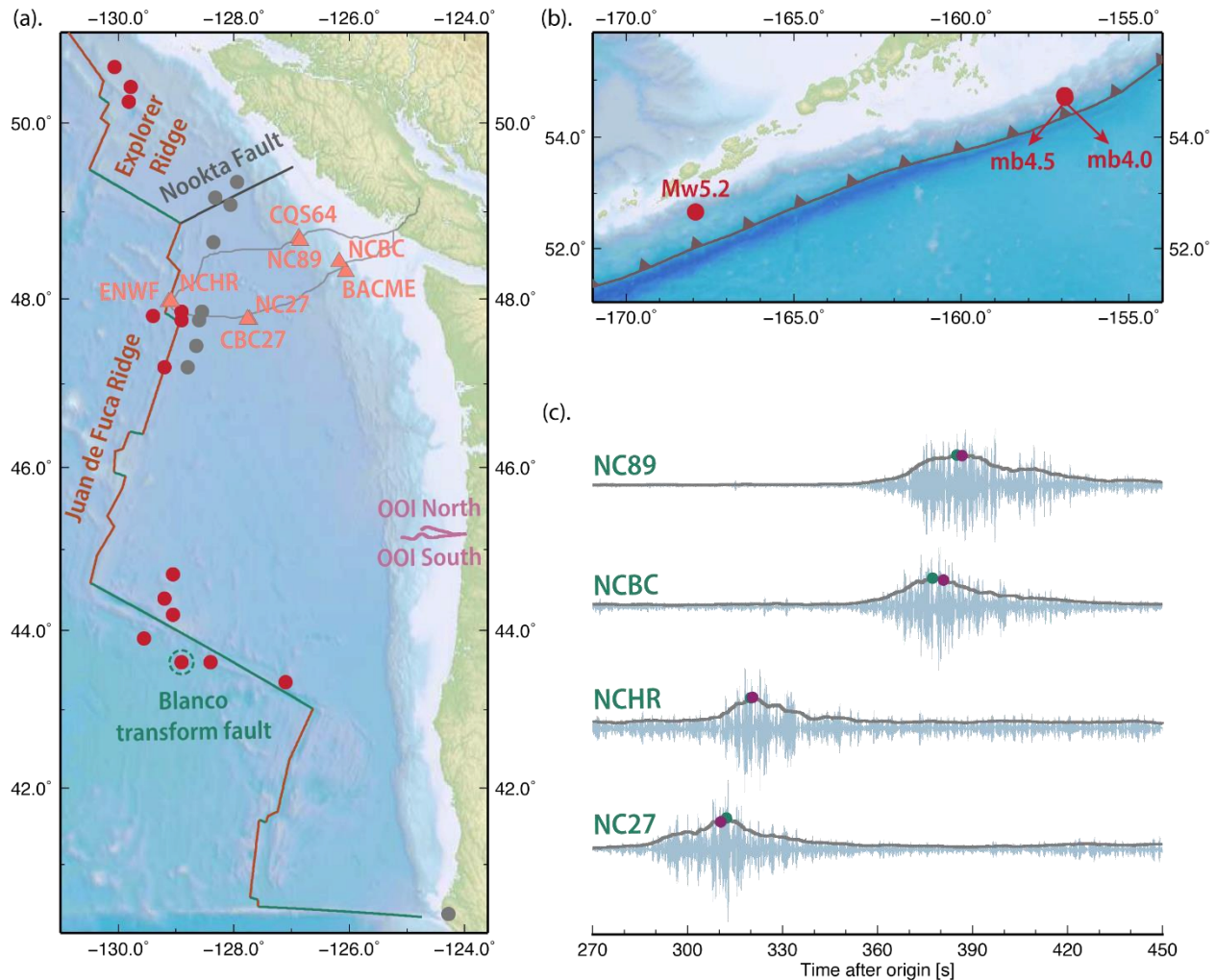
141 seismic, oceanographic, acoustic, and geodetic processes (Wilcock et al., 2023). Specifically,  
142 between November 1<sup>st</sup> and 5<sup>th</sup>, two fiber-optic backbone cables were temporarily converted to  
143 OBDAS arrays, referred to as OOI North and OOI South. The OOI North array had two optical  
144 fibers connected to Optasense QuantX and Silixa iDASv3 interrogators, respectively, to record  
145 OBDAS data up to the first optical repeater located at ~65 km from the shore, with a gauge length  
146 of 30 m during most of the experiment. OOI South had one fiber for collecting OBDAS data using  
147 another Optasense QuantX interrogator, while the other fiber was used for distributed temperature  
148 sensing. The first optical repeater of OOI South is located ~95 km away, and the gauge length is  
149 set at 50 m. With a channel spacing of ~2 m, the OOI North array has a total number of 32,600  
150 channels whereas the OOI South array consists of 47,500 channels. During the experiment, both  
151 arrays recorded abundant low-frequency acoustic signals such as whale calls and ship noise  
152 (Wilcock et al., 2023). In this study, we solely focus on the Optasense OBDAS data since the data  
153 from both arrays are available, allowing for a direct and straightforward comparison.

154 Located ~400 km northeast of the RCA network, the Ocean Networks Canada (ONC) North-East  
155 Pacific Undersea Networked Experiments (NEPTUNE) off the coast of British Columbia is  
156 another multidisciplinary observatory that has been used to monitor the earth/ocean system since  
157 2009. The NEPTUNE network consists of more than 14 ocean bottom seismometers,  
158 accelerometers and hydrophones that are mainly distributed across four sites: Clayoquot Slope,  
159 Endeavour Ridge, Cascadia Basin, and Barkley Canyon (Barnes et al., 2008; Figure 1b). Both the  
160 OOI and NEPTUNE networks have high sensitivity to *T*-waves from earthquakes at mid-ocean  
161 ridges and transform faults in the northeast Pacific and the Aleutian subduction zone (Dziak et al.,  
162 2012; Tréhu et al., 2018).

### 163 **3 Regional *T*-wave event catalog using NEPTUNE**

164 During the four-day community DAS experiment, the global ISC (International Seismological  
165 Centre; Bondár & Storchak, 2011) catalog only documents a few earthquakes in the northeast  
166 Pacific that might produce high-quality *T*-waves (Table S1). To search for a more complete set of  
167 *T*-wave events, we download vertical component seismograms from eight NEPTUNE stations,  
168 with two at each site (Figure 2a), remove their instrument responses, mean values and linear trends,  
169 and band-pass filter the data between 4 and 6 Hz, which is favorable for high-quality *T*-wave  
170 observations (Okal, 2008). We implement a recursive short-time-average/long-time-average  
171 (STA/LTA) algorithm (Withers et al., 1998) to detect *T*-waves on each individual station. With a  
172 STA of 5 s and LTA of 50 s, potential *T*-waves are identified once their STA/LTA ratios exceed a  
173 threshold of 1.8, which corresponds to ~12 times the median absolute deviation of daily STA/LTA.  
174 We then clean all the picks in a 50-s sliding window and only retain detections if *T*-waves are  
175 observed at more than three sites (Figure 2c). After careful visual examinations, we establish a  
176 total of 27 *T*-wave events (Table S1). Our NEPTUNE catalog includes six earthquakes in the ISC  
177 catalog with three M4.0+ events in the Aleutian trench, two small ones north of NEPTUNE and a

178 Mw4.4 event near the coast of Northern California (Figure 2; Table S1), confirming the robustness  
 179 of our method.



180  
 181 **Figure 2.** Ocean Networks Canada NEPTUNE  $T$ -wave catalog. (a). Regional seismicity detected  
 182 using  $T$ -waves at the NEPTUNE networks. The red and gray circles indicate earthquakes with  
 183 detectable and undetectable  $T$ -waves on OOI OBDAS, respectively. The green dashed circle  
 184 denotes the event shown in (c). (b). Similar to (a) but for earthquakes along the Aleutian trench.  
 185 (c).  $T$ -waves detected on the NEPTUNE array from a Blanco earthquake. The gray lines indicate  
 186  $T$ -wave envelopes smoothed by a 5-s sliding window. The green and purple solid circles represent  
 187 the picked and predicted  $T$ -wave arrivals (envelope peaks), respectively.

188 We find four non-ISC events that generate clear  $P$ -waves and  $S$ -waves at nearby onshore stations  
 189 (Figure S1). To determine their origin times and locations, we perform a grid search with an  
 190 interval of  $0.02^\circ$ , minimizing the L1 norm of the time differences between predicted and manually  
 191 picked  $P$  and  $S$  arrivals (see supplementary text S1 for more details; Kennett & Engdahl, 1991).  
 192 All of them are located in regions of active background seismicity close to the continental shelf –

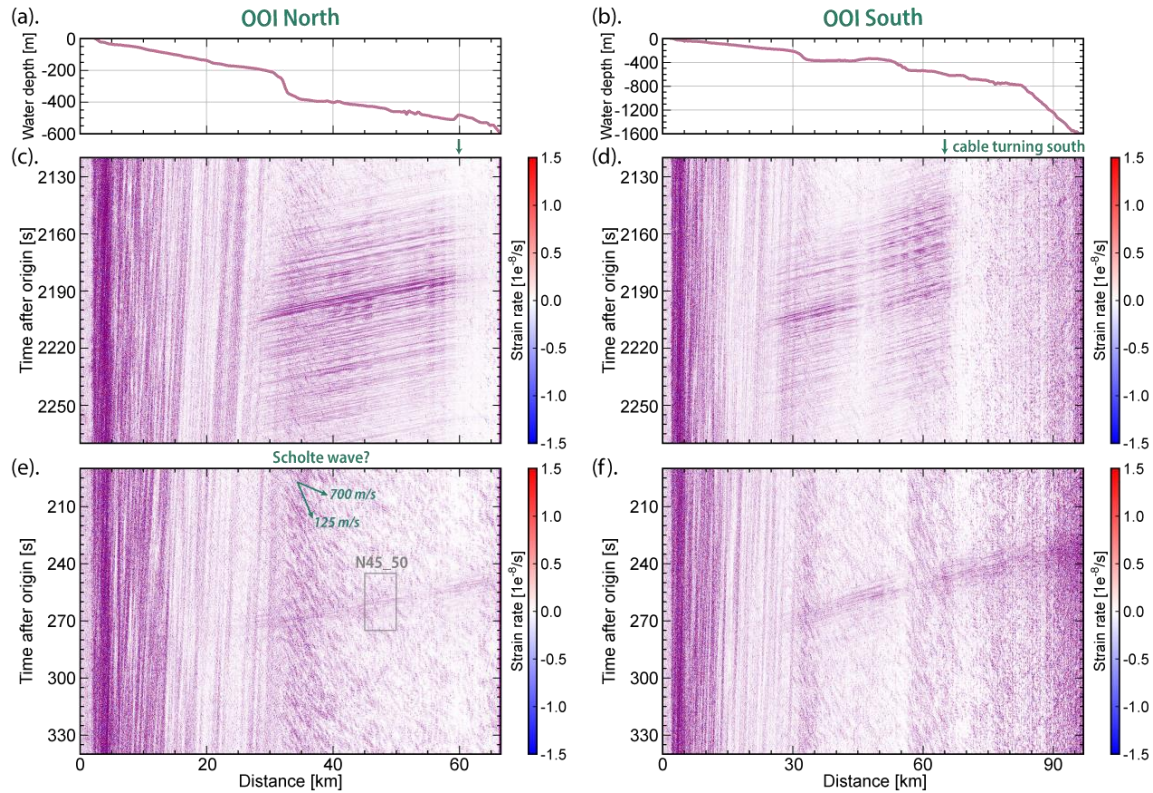
193 two near the Explorer Ridge and the other two to the north of the NEPTUNE array (Figures 2a and  
194 S1). Given the optimal locations, we estimate their local magnitudes (ML) by averaging over all  
195 the stations in a frequency band of 2-10 Hz (Bakun & Joyner, 1984). The resulting magnitudes,  
196 ranging from ML1.6 to ML2.3, are too small to be detected in the ISC catalog (Table S1). For the  
197 remaining non-ISC events without clear P and S observations at onshore stations, we use the arrival  
198 times of *T*-wave envelope peaks to determine event locations (Figures 2c and S1). Compared to  
199 *P*-waves and *S*-waves, *T*-waves are excited within a broad area near the source (Okal, 2008) and  
200 consequently less sensitive to earthquake locations, so we limit the grid search to seismically active  
201 regions and use a relatively larger interval of  $0.05^\circ$ . Given that oceanic earthquakes are typically  
202 shallow and *T*-wave arrival time has little sensitivity to depth, the focal depth is fixed at 10 km.  
203 The results suggest that most events reflect local seismicity near the NEPTUNE array (Hyndman  
204 et al., 1979; Hooft et al., 2010; Savard et al., 2020) but seven of them are from the Blanco transform  
205 fault (Table S1), all of which are consistent with the tectonic background (Figure 2a). We do not  
206 determine the magnitudes of the seven Blanco events since a robust magnitude estimate using *T*-  
207 wave is challenging (Okal, 2008). However, a previous study by Fox et al. (1993) suggested that  
208 detectable *T*-wave events at similar distances are generally of magnitude M2.0+. Overall, our four-  
209 day catalog includes many more events compared to the global ISC catalog and provides us with  
210 prior knowledge to search for *T*-waves on OOI OBDAS.

## 211 **4 OBDAS for *T*-wave observations and denoising**

### 212 **4.1 *T*-wave observations at OOI OBDAS**

213 With the new catalog, we visually scrutinize the *T*-waves on OBDAS for each event at 4-6 Hz, the  
214 same frequency band used for the NEPTUNE *T*-wave observations. Most of the events, except for  
215 those near the NEPTUNE array, excite visible *T*-waves at OOI North and OOI South (Figure 2;  
216 Table S1). In particular, a Mw5.2 Fox islands earthquake, the largest event in our NEPTUNE  
217 catalog, generates clear *T*-waves with a duration of >150 s on the 25-60 km portion of OOI North  
218 (N25\_60) and 20-65 km segment of OOI South (S20\_65; Figures 3c and 3d). Intriguingly, the  
219 wavefields exhibit a sharp drop of *T*-wave energy at distances of ~60 km on OOI North and ~65  
220 km on OOI South (Figure 3), where the cable orientations become more perpendicular to the *T*-  
221 wave propagation direction (Figure 1b). The decreases in *T*-wave energy could be attributed to the  
222 directional sensitivity of OBDAS – the radial strain converted from the acoustic pressure of a *T*-  
223 wave would be reduced when the incoming wave propagation direction becomes perpendicular to  
224 the cable orientation (Martin et al., 2021; Fang et al., 2023). Another possible explanation for the  
225 weaker *T*-wave observation could be elevated bathymetry blocking the wave propagation to the  
226 seafloor. However, the latter interpretation may not be applicable here as no obvious elevated  
227 bathymetry is present. In contrast, earthquakes from the Blanco transform fault exhibit more  
228 continuous *T*-wave wavefields across both cables (Figures 3e and 3f), favoring our former  
229 interpretation of directional sensitivity. Compared to the Mw5.2 Fox islands earthquake, the

230 Blanco event produces  $T$ -waves with shorter durations and lower signal-to-noise ratios (SNR) due  
 231 to its smaller magnitude (Figure 3). In both cases,  $T$ -waves consistently exhibit lower SNRs at  
 232 cable distances less than 30 km (Figure 3), which can be attributed to two main factors. Firstly, the  
 233 presence of strong background noise associated with ocean gravity waves significantly  
 234 contaminates the  $T$ -wave signal. Secondly, as the  $T$ -wave propagates towards the coast, it  
 235 undergoes complex interactions with the seafloor, leading to dramatic signal attenuation.

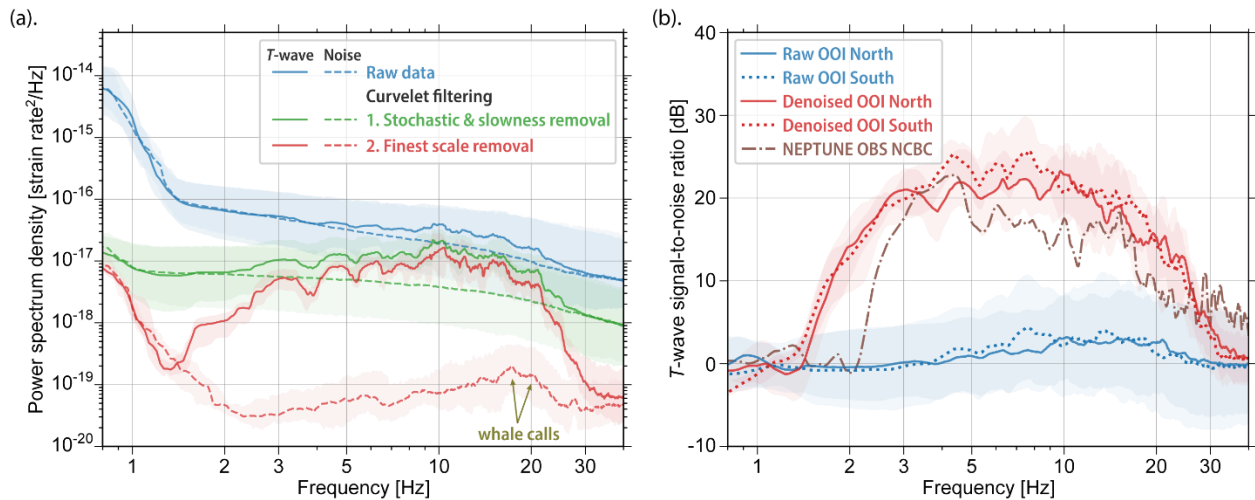


236

237 **Figure 3.** 4-6 Hz  $T$ -waves on the OOI OBDAS arrays. (a). Water depth along OOI North. (b).  
 238 Water depth along OOI South. (c). The 4-6 Hz  $T$ -wave on OOI North from the Mw5.2 Fox islands  
 239 earthquake. (d). Similar to (c) but for OOI South. (e). The 4-6 Hz  $T$ -wave on OOI North from a  
 240 Blanco earthquake that occurred on November 4<sup>th</sup>, 2021 (dashed circle in Figure 2a; Event No. 25  
 241 in Table S1). The grey box N40\_45 denotes the wavefield used in Figures 4 and 6. (f). Similar to  
 242 (e) but for OOI South.

243 As a relatively new instrument for underwater environment, OBDAS can in fact record  $T$ -waves  
 244 across a broad frequency band, extending beyond the 4-6 Hz range, but with lower SNRs. Taking  
 245 the Blanco earthquake as an example, we calculate the noise and  $T$ -wave spectra of individual  
 246 OBDAS channels on the 45-50 km segment of OOI North (N45\_50; Figure 3e). Given a sound  
 247 speed of 1.5 km/s, we select the noise and  $T$ -wave windows as -45 to -15 s and -15 to 15 s relative  
 248 to the predicted  $T$ -wave arrivals, respectively. The resulting power spectrum density (PSD) of raw  
 249 OBDAS data exhibits large amplitude noise below 1 Hz, likely associated with ocean-related  
 250 microseisms (Webb, 1998; Figure 4a). The PSD then sharply drops at 1-2 Hz and gradually decays

251 from 2 Hz to 40 Hz (Figure 4a), which is consistent with previous observations (Lior et al., 2021;  
 252 Ugalde et al, 2022). The median PSD of the *T*-wave is slightly above the median PSD of noise  
 253 between 4 Hz and 30 Hz, resulting in a low *T*-wave SNR up to  $\sim 3$  dB at 10-20 Hz (Figure 4). OOI  
 254 South also exhibits similar *T*-wave observations, while the NEPTUNE OBS at a similar water  
 255 depth but a larger distance shows one order of magnitude higher SNRs over a broad frequency  
 256 range (2-40 Hz) peaking at 3-5 Hz (Figure 4b). The low SNRs in OOI OBDAS are due to  
 257 significant noise masking the landward propagating *T*-wave. The noise is predominantly grouped  
 258 in the seaward direction with a slowness range of 125-700 m/s, which is likely associated with  
 259 Scholte waves backscattered from a bathymetry step at  $\sim 30$  km on OOI North (Figure 3e). Previous  
 260 OBDAS studies also reported backscattered Scholte waves in ambient noise cross-correlations and  
 261 attributed them to subsurface lateral variations (Spica et al., 2020; Cheng et al., 2021). Here, our  
 262 observations of backscattered Scholte waves are likely linked with the sharp change of bathymetry  
 263 as supported by their consistent presence on both OOI OBDAS arrays (e.g.,  $\sim 30$  km and  $\sim 60$  km  
 264 at OOI South; Figure 3).



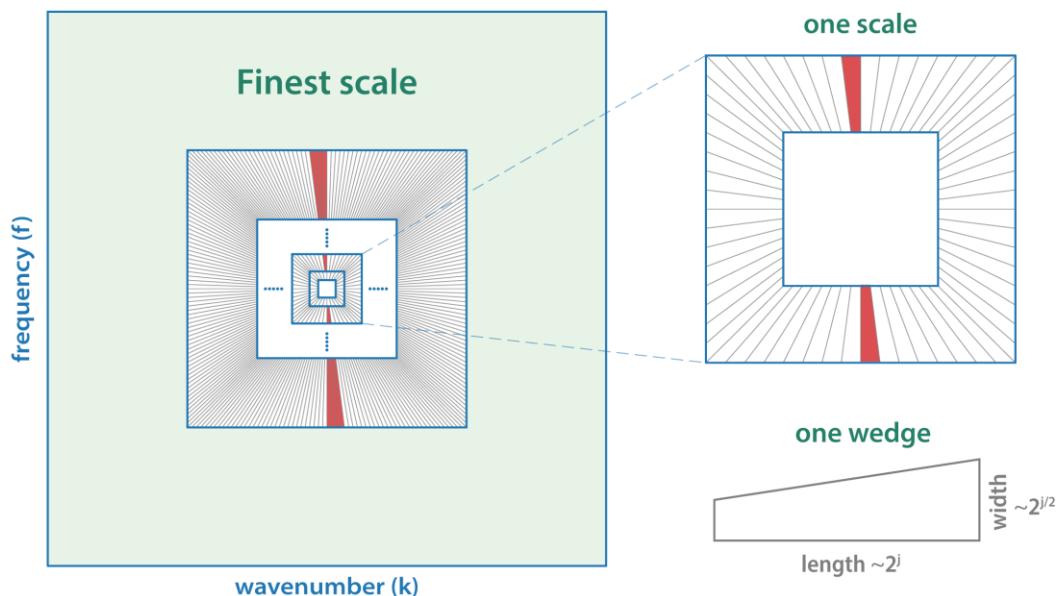
265

266 **Figure 4.** Power spectral density and SNR of a *T*-wave at the OOI OBDAS and a NEPTUNE OBS  
 267 station. (a). Strain rate PSD of raw data and curvelet filtered data at N45\_50. The solid lines denote  
 268 the median PSDs of a *T*-wave across N45\_50. The dashed lines correspond to the median PSDs of  
 269 noise. The curves are color-coded to display the outcomes resulting from successive curvelet  
 270 denoising steps. The shadow areas represent the 10th to 90th percentiles of corresponding PSDs  
 271 obtained from individual channels at N45\_50. (b). *T*-wave SNRs at OOI North (N45\_50), OOI  
 272 South (S50\_55), and NEPTUNE station NCBC as a function of frequency. The SNR curves plotted  
 273 for OBDAS represent the median SNRs of individual channels. The associated shadow areas  
 274 correspond to the 10th to 90th percentiles of PSDs obtained from individual channels. N45\_50,  
 275 S50\_55, and NCBC are at a similar water depth of  $\sim 400$  m.

276

## 4.2 Curvelet denoising

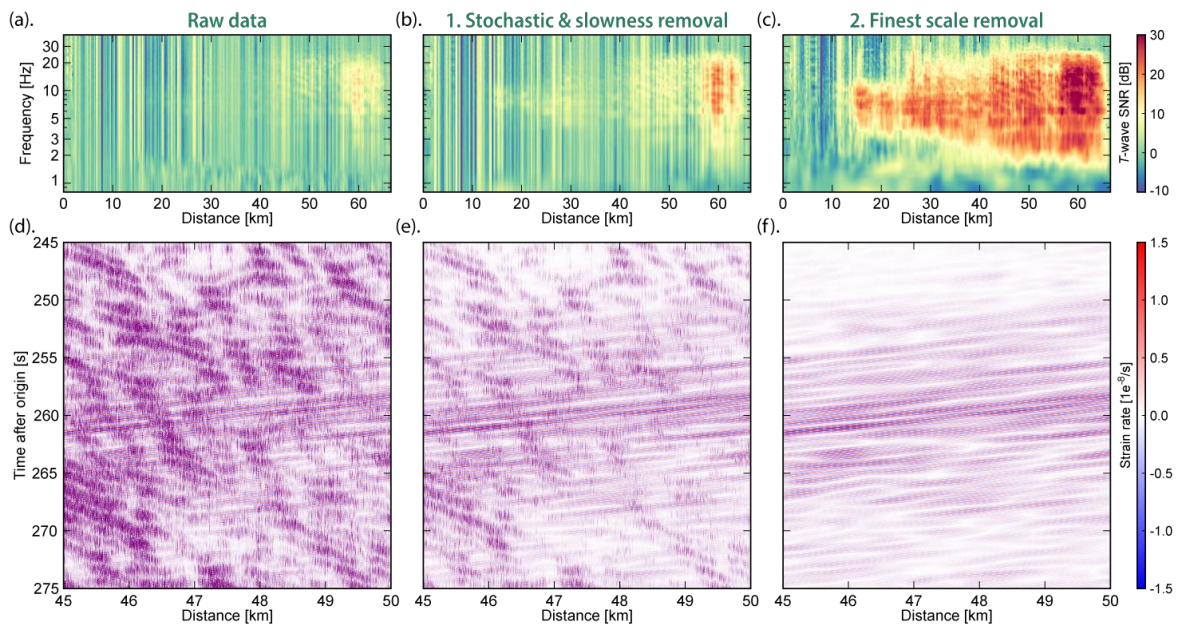
277 We adopt a curvelet denoising approach to enhance *T*-wave SNRs by taking advantage of  
 278 waveform coherence across dense OBDAS channels. Curvelets are designed to optimally represent  
 279 images with a finite number of geometric discontinuities along twice continuously differentiable  
 280 curves, which is a desirable tool for DAS data with the *T*-wave acting as bounded curvature  
 281 (Candès & Donoho, 2004). Compared to classic Fourier and wavelet transforms, the curvelet  
 282 transform is a tight frame that enables the reconstruction of an image with a series of curvelets  
 283 weighted by their coefficients but is better suited to preserving directional features through a polar  
 284 tiling of the frequency-wavenumber (*f*-*k*) domain (Candès et al., 2006). For practical applications  
 285 with discrete data (e.g., OBDAS seismic data), the curvelet transform is usually implemented in a  
 286 discrete frame using Cartesian counterparts of the polar tiling. Explicitly, the *f*-*k* plane is  
 287 partitioned into a range of concentric scales dictated by dyadic squares whose width doubles every  
 288 scale (Figure 5). Each scale is further compartmentalized by slowness into a set of parabolic  
 289 angular wedges, which correspond to needle-shaped wave packets or mother curvelets in the time  
 290 domain (Figure 5). Due to the parabolic scaling, the number of wedges doubles every other scale,  
 291 and the mother curvelets consequently become more needle-like at finer scales. In this manner, the  
 292 curvelet transform presents a high degree of localization in position, frequency, and orientation,  
 293 and thus has been exploited in seismology for seismic denoising (Hennenfent & Herrmann, 2006),  
 294 wavefield reconstruction (Jack & Zhan, 2021), and seismic phase augmentation (Yu et al., 2017;  
 295 Zhang & Langston, 2020).



296

297 **Figure 5.** Schematic curvelet tiling of the frequency-wavenumber domain. The right panels are  
 298 examples of the third scale and a parabolic angular wedge. Red wedges denote the wedges  
 299 associated with *T*-wave slowness and thus are retained during the slowness removal.

300 Recently, Atterholt et al. (2022) proposed a unified wavefield-partitioning approach for  
 301 simultaneously removing stochastic and coherent noise (e.g., traffic signals) for DAS on land.  
 302 Under the curvelet frame, stochastic noise can be removed by implementing a soft thresholding to  
 303 curvelet coefficients, which involves zeroing the curvelet coefficients below a noise threshold and  
 304 subtracting the threshold from those above it. The effect of slowness removal for coherent noise  
 305 is to mute angular wedges associated with the noise slowness. We follow a similar scheme and  
 306 apply stochastic and slowness removal to OOI North for the Blanco example. We adopt a  
 307 wrapping-based fast discrete curvelet transform algorithm for computational efficiency and assign  
 308 wavelets to facilitate the implementation of appropriate basis functions at the finest scale (Candès  
 309 et al., 2006). Unlike DAS on land, the noise level and  $T$ -wave energy of OBDAS exhibit significant  
 310 lateral variation dependent on water depth and bathymetry (Figure 3). Therefore, we implement a  
 311 spatially dependent soft thresholding by taking cable location into account. Specifically, we cut a  
 312 180-s window before the  $T$ -wave arrival as a noise window and take the curvelet transform of it.  
 313 For each curvelet, its coefficient matrix describes the corresponding noise level in both temporal  
 314 and spatial dimensions. By rolling along the cable, we set the threshold as the 70th percentile of  
 315 the coefficient matrix at each cable location. In slowness removal, we only retain the curvelets  
 316 associated with  $T$ -waves propagating towards the shore at an apparent speed faster than  $\sim 1.0$  km/s.  
 317 Indeed, the stochastic and slowness removal improves  $T$ -wave SNRs at individual channels and  
 318 suppresses the coherent noise moving seaward (Figures 6a/6d vs 6b/6e). Consequently, the median  
 319 PSD of the stochastic and slowness filtered  $T$ -wave exceeds the noise level at low frequencies (e.g.,  
 320 2-4 Hz; Figure 4a).



321

322 **Figure 6.** Illustration of curvelet denoising for enhancing  $T$ -wave SNRs on OBDAS. (a).  $T$ -wave  
 323 SNRs of individual OBDAS channels in OOI North. (b).  $T$ -wave SNRs after stochastic denoising  
 324 and slowness removal. (c).  $T$ -wave SNRs after an additional finest-scale removal. (d). The 4-6 Hz

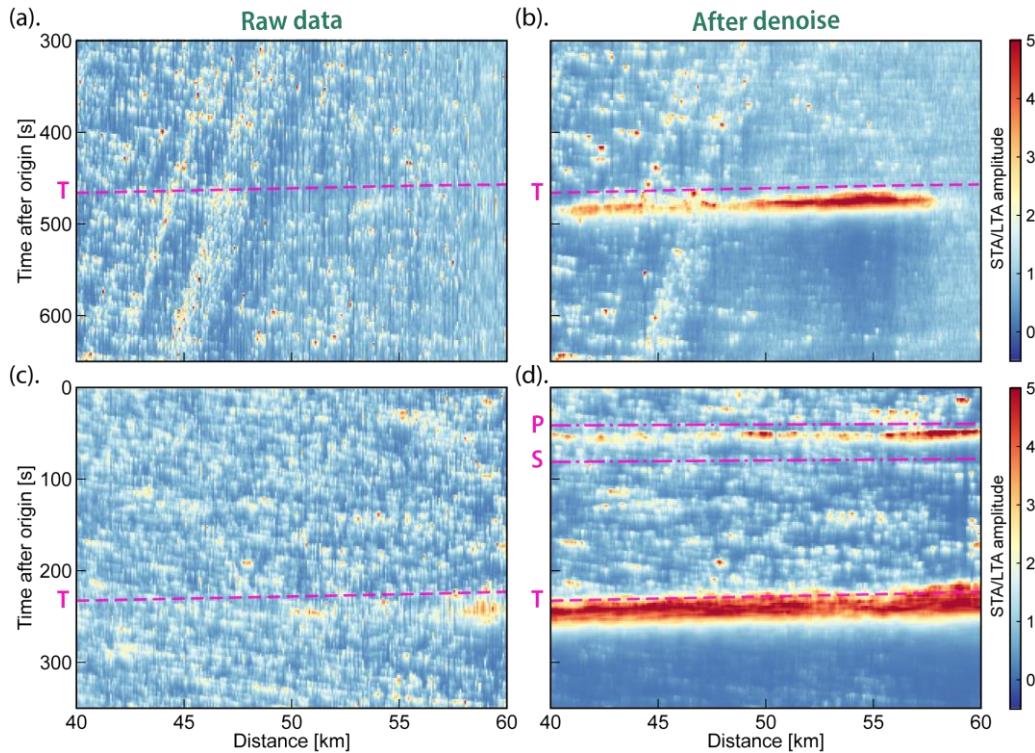
325 OBDAS wavefield at N45\_50 in Figure 3e. (e). The 4-6 Hz OBDAS wavefield after stochastic and  
326 slowness removal. (f). Similar to (e) but after an additional finest-scale removal.

327 Despite the application of stochastic and slowness denoising, there is certain spiky noise in the  
328 data that cannot be effectively removed. The spiky noise demonstrates very low coherency and,  
329 therefore, unlikely corresponds to *T*-waves or any natural signals (Figure 6e). Upon thorough  
330 examination, we find that these spiky artifacts are primarily concentrated in the finest scale of the  
331 *f*-*k* domain. Thus, to further improve *T*-wave SNRs, we implement an additional finest-scale  
332 removal approach by zeroing out all the coefficients at finest scale (Figures 6c and 6f). As a result,  
333 the median PSD abruptly drops to  $\sim 10^{-19}$ , which is 2-3 orders of magnitude smaller than that of the  
334 original data (Figure 4a). Intriguingly, we observe that a small PSD peak emerges around 20 Hz  
335 in our noise time window, which has been suggested to be associated with whale calls (Wilcock  
336 et al., 2023; Figure 4a). After denoising, the median *T*-wave SNRs of OOI North and OOI South  
337 can reach up to  $\sim 25$  dB over a broad frequency band spanning from 1.5 Hz to 30 Hz, slightly  
338 outperforming a NEPTUNE OBS at a similar water depth (Figure 4b).

## 339 **5 OBDAS for oceanic seismicity detection and location**

### 340 **5.1 detecting *T*-wave events**

341 Curvelet denoising effectively enhances *T*-wave signals, enabling us to detect small *T*-wave events  
342 hidden in the noise. To illustrate, we select two representative events from the NEPTUNE *T*-wave  
343 catalog (i.e., Event No. 5 and 27 in Table S1). The first event with a small magnitude of ML1.7  
344 occurred near the Explorer ridge, which is about 460 km away from OOI North. The other event  
345 at the Blanco transform fault is at a shorter distance of  $\sim 240$  km. We apply the recursive STA/LTA  
346 algorithm to detect *T*-waves in a frequency band of 5-10 Hz on the 40-60 km segment of OOI  
347 North (N40\_60), which has relatively high SNRs along the cable (Figure 3). However, both events  
348 are too small to produce detectable *T*-wave signals in the raw data. Consequently, the STA/LTA  
349 approach fails to trigger a detection for the *T*-wave (Figures 7a and 7c), except for a small portion  
350 of the cable (e.g., at  $\sim 50$  and  $\sim 60$  km) where STA/LTA amplitudes slightly are higher than the  
351 background levels at the predicted *T*-wave arrival times of the Blanco event (Figure 7c). After  
352 denoising, *T*-waves become evidently visible across N40\_60 for both events (Figures 7b and 7d),  
353 underscoring the great seismic monitoring potential of OBDAS. In addition, curvelet denoising  
354 also substantially enhances the *P*-wave from the Blanco earthquake while the *S*-wave remains  
355 undetected (Figure 7d).



356

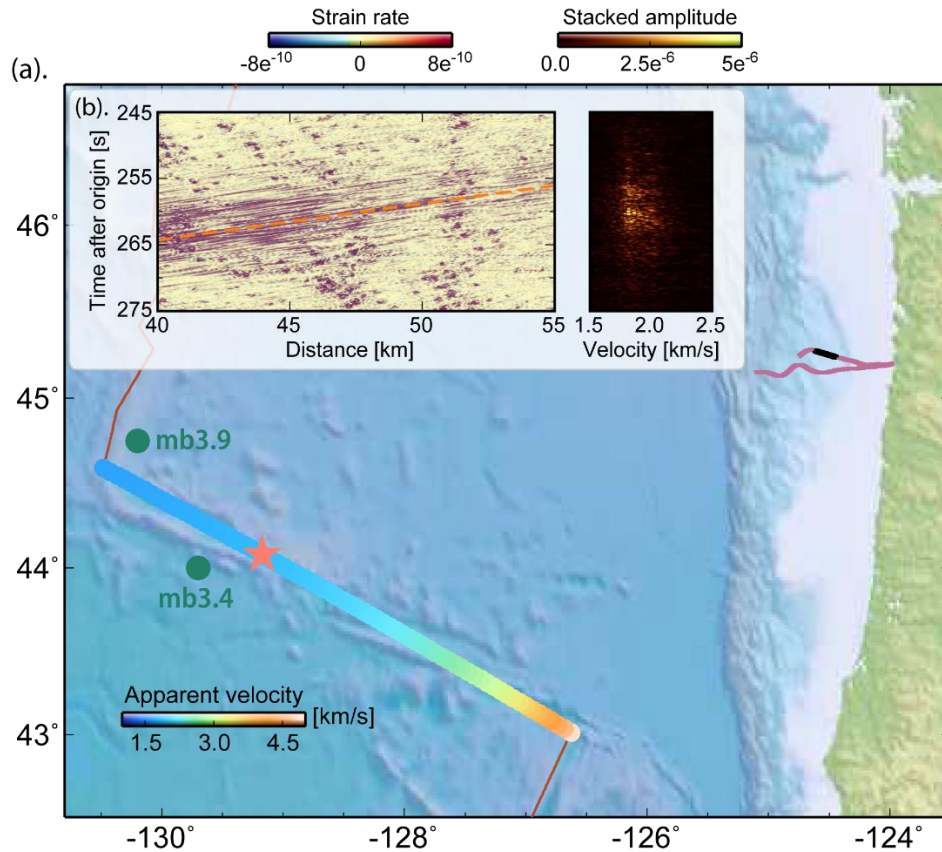
357 **Figure 7.** Illustration of curvelet denoising for enhancing  $T$ -wave detectability of OBDAS. (a).  
 358 STA/LTA results for 5-10 Hz raw OBDAS data of the ML1.7 earthquake on November 2nd, 2021  
 359 (Event No. 5 in Table S1). (b). Similar to (a) but for denoised data. (c). STA/LTA detections using  
 360 5-10 Hz raw OBDAS data of the Blanco earthquake on November 5th, 2021 (Event No. 27 in  
 361 Table S1). (d). Similar to (c) but for curvelet denoised data.

362 The evident effectiveness of curvelet denoising in these two small earthquakes motivates us to  
 363 investigate the potential of OBDAS for long-term  $T$ -wave detection. We use the complete 4-day  
 364 dataset of N40\_60, downsample the data to 50 Hz, divide them into 10-min windows, and apply  
 365 curvelet denoising and recursive STA/LTA. We average the STA/LTA over all channels with a  
 366 velocity correction of 1.5 km/s. An event is detected if the averaged STA/LTA amplitude exceeds  
 367 a threshold of 1.5, similar to the NEPTUNE  $T$ -wave catalog. After visual scrutinization to remove  
 368  $P$ -waves and false detections, we document a total of 92  $T$ -wave events for OOI North. Compared  
 369 to the NEPTUNE  $T$ -wave catalog, our new OOI North  $T$ -wave catalog includes 17 of the 27  
 370 NEPTUNE events. The missed 10 events are local seismicity near the NEPTUNE array (gray  
 371 circles in Figure 2), which are probably too small to be detected at OOI North. Meanwhile, OOI  
 372 North identifies 2-3 times more earthquakes than the NEPTUNE array in the first half of the  
 373 experiment (Figure 8). The excess  $T$ -wave events on OOI North are likely associated with  
 374 aftershocks of a mb3.9 Blanco earthquake or a mb3.4 Blanco earthquake that both occurred on  
 375 November 1<sup>st</sup>, 2021 (Figure 9), right before the experiment. The  $T$ -wave detection rate of OOI  
 376 North gradually decreases from 6-8 events per 4 hours on November 2<sup>nd</sup> to 1-4 events per 4 hours  
 377 on November 4<sup>th</sup> and 5<sup>th</sup>. This declining trend could be partially attributed to an increase in the



402 slopes are observed compared to the cable section beyond 55 km (Figure S2). This implies that the  
403 <55 km cable section exhibits higher sensitivity to azimuthal constraints of Blanco events.  
404 Therefore, we choose the N40\_55 km segment—a region marked by high sensitivity to source  
405 location and high *T*-wave SNRs—to compute the apparent velocity and infer the back azimuth of  
406 a Blanco event detected by OBDAS.

407 Indeed, the theoretical *T*-wave arrival times along the N40\_50 segment from Blanco earthquakes  
408 unveil a discernible pattern of location-dependent apparent velocity (Figures 9). The apparent  
409 velocity gradually increases from 1.5 km/s to 5 km/s as an earthquake moves eastward along the  
410 Blanco transform fault (Figure 9), allowing for source azimuth estimation. Taking a Blanco event  
411 that occurred at 00:05 on November 2<sup>nd</sup>, 2021, as an example, a slant stack of its *T*-waves at  
412 N40\_55 exhibits an amplitude peak at an apparent velocity of 1.82 km/s, which corresponds to a  
413 back azimuth of 252° given a propagation speed of 1.5 km/s (Figure 9). The resolved back azimuth  
414 intercepts the Blanco fault trace at a location of 44.08°N, 129.17°W. The Blanco example is close  
415 to our relocated mb3.4 Blanco event that occurred at 2021-11-01T12:59, right before the OOI  
416 community experiment, suggesting that it could be an aftershock of the mb3.4 event. With this  
417 location, we calculate the theoretical *T*-wave arrival times at two NEPTUNE stations, which align  
418 reasonably well with observed data (Figure S3). Meanwhile, compared to the mb3.9 and mb3.4  
419 events, the *T*-wave amplitudes of our Blanco event example are one order of magnitude weaker at  
420 the same station (Figure S3), indicating a relatively small magnitude. However, only OOI North  
421 is used in this example, leaving the epicenter distance unresolved. Looking forward, an optimal  
422 approach to determine the source location would involve integrating travel time and slowness data  
423 from all available instruments, including OBDAS, *T*-wave stations, and hydrophones from a wide  
424 range of azimuths.



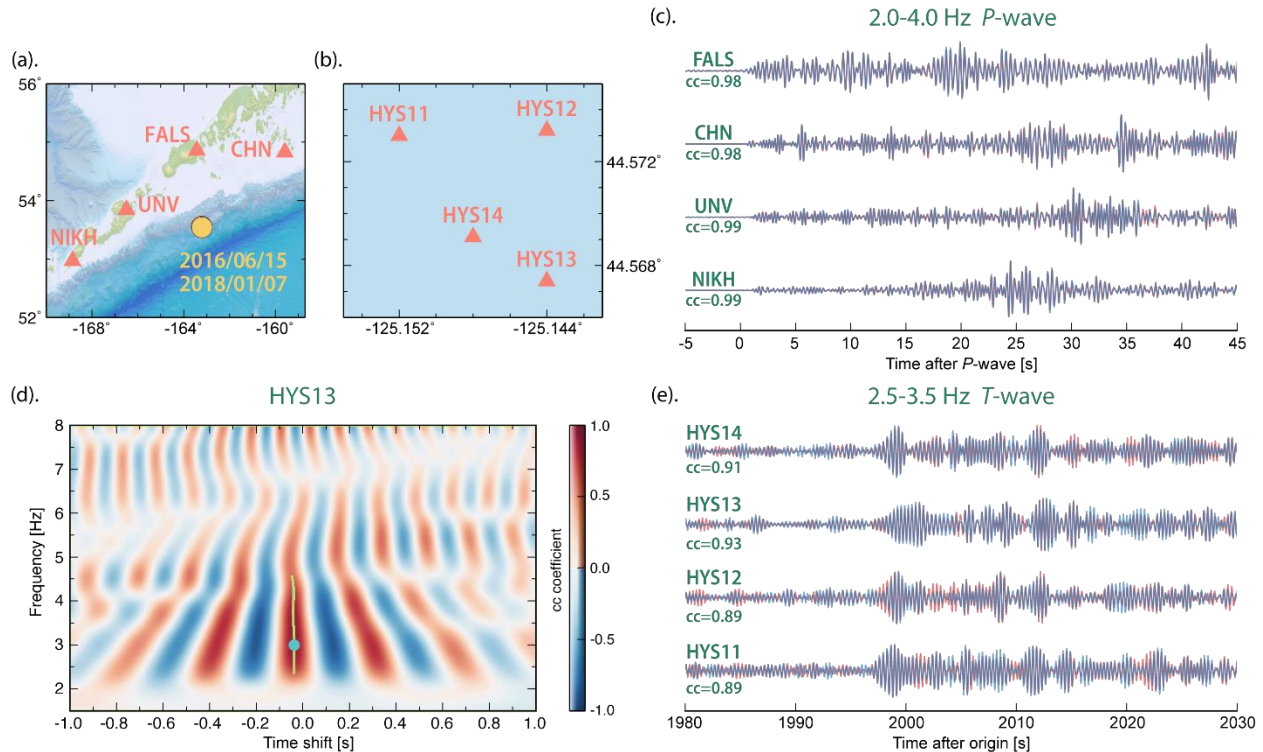
425

426 **Figure 9.** Locating the 2021-11-02T00:05 Blanco earthquake using *T*-waves on OOI North. (a).  
 427 Slowness sensitivity of OOI North *T*-wave to earthquake location. The color along the Blanco  
 428 transform fault shows predicted *T*-wave slowness at N40\_55 (black line), corresponding to  
 429 different earthquake locations along the fault. The green circles and red star denote the relocated  
 430 mb3.9, mb3.4 and estimated location of the 2021-11-02T00:05 event, respectively. (b). *T*-waves  
 431 at 5-10 Hz and slant stack results. The orange dashed line represents the *T*-wave apparent velocity  
 432 of 1.82 km/s.

### 433 6 OBDAS for seismic ocean thermometry

434 The improved SNRs of *T*-waves through denoising also helps enhance the feasibility of OBDAS-  
 435 based seismic ocean thermometry, allowing a larger number of small repeating earthquakes to be  
 436 employed for SOT. In the Northeast Pacific, the abundant seismicity along the Aleutian subduction  
 437 zone can generate high-quality *T*-waves propagating to the OOI OBS array. Following Wu et al.  
 438 (2020), we identify two repeating earthquakes, on June 15<sup>th</sup>, 2016 and January 7<sup>th</sup>, 2018, near the  
 439 epicenter of the Mw5.2 Fox Islands earthquake. They exhibit almost identical *P*-waves at four  
 440 local stations (Figure 10c). The corresponding *T*-waves at OOI OBSs HYS11-14 also show high  
 441 cross-correlation (CC) coefficients of  $\sim 0.90$  in a frequency band of 2.5-3.5 Hz (Figure 10e). The  
 442 CC coefficient gradually drops as the frequency increases (Figure 10d), that is similar to the  
 443 previous observations in the Indian Ocean (Callies et al., 2023; Wu et al., 2023). Taking a CC

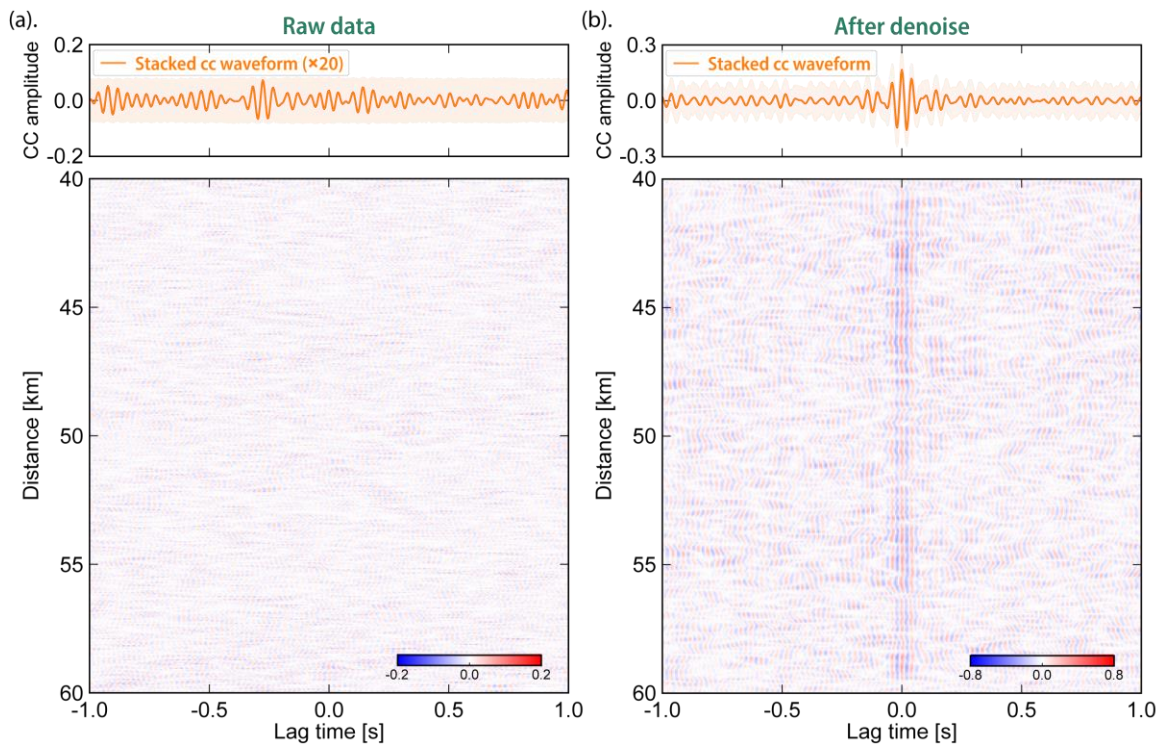
444 coefficient threshold of 0.6, the  $T$ -wave travel time shifts between 2.35 Hz and 4.6 Hz would be  
 445 used to infer average ocean temperature change along the  $T$ -wave path. In this example, the slight  
 446  $T$ -wave travel time shift of -0.04 s at 3 Hz (Figure 10d) indicates a weakly warming ocean averaged  
 447 over the top 3 km of the water column along the  $\sim$ 3000 km source-receiver path (see supplementary  
 448 text S2 and Figure S4 for more details; Komatitsch & Tromp, 1999; McDougall & Barker, 2011;  
 449 Forget et al., 2015).



450  
 451 **Figure 10.** Illustration of SOT concept using repeating earthquakes in the Aleutian trench and OOI  
 452 OBSs. (a). The map of repeating earthquakes and local stations at the Aleutian trench. (b). The  
 453 map of OOI OBS array. (c).  $P$ -waves of the 15 June 2016 event (red) and 7 January 2018 (blue)  
 454 event. The station names and CC coefficients are indicated on the left.  $P$ -waves from the 2016  
 455 event are synchronized based on their predicted arrivals at each station using the ISC source  
 456 parameters. The  $P$ -waves from the 2018 event are aligned with the corresponding 2016  $P$ -waves  
 457 using waveform cross correlation. (d). Frequency dependent  $T$ -wave CC results of HYS13. The  
 458 green line indicates the frequency-dependent time shifts measured by tracking the stripe of peak  
 459 CC coefficient above 0.6. The green dot shows a time shift of -0.04 s measured at 3 Hz. (e).  $T$ -  
 460 waves at the four OOI OBSs. The relative origin time error between the 2016 event and 2018 event  
 461 is corrected using the  $P$ -waves shown in (c).

462 Within the limited 4-day experiment period, we do not find any natural repeating earthquake pair  
 463 in the Northeast Pacific region producing  $T$ -waves usable for SOT. Thus, we generate pseudo-  
 464 repeating earthquakes to evaluate the SOT performance of OBDAS by incorporating realistic noise  
 465 data into the  $T$ -waves of the Mw5.2 Fox Islands earthquake. Specifically, we randomly select 20

466 three-minute noise data segments from OOI North and superimpose each of these noise segments  
 467 onto magnitude-calibrated  $T$ -waves. To perform the calibration, we assume a circular crack model  
 468 and constant stress drop (Madariaga, 1976; Allmann & Shearer, 2009). Based on this assumption,  
 469 the  $T$ -wave amplitude would be proportional to  $M_0^{2/3}$ , where  $M_0$  represents the seismic moment.  
 470 For instance, a decrease in the moment magnitude by one-unit results in a 10-fold drop of  $T$ -wave  
 471 amplitude. With the scaling, we generate pseudo-repeating OBSDAS  $T$ -waves for a given  
 472 magnitude, perform curvelet denoising, and evaluate the performance of OBSDAS for SOT. We  
 473 use the OBDAS data at N40\_60 for illustration. It is important to point out that applying stochastic  
 474 removal independently to each pseudo-repeating event can lead to inconsistent zeroing of noisy  
 475 curvelet coefficients and compromise the accuracy of  $T$ -wave time shifts. To ensure a consistent  
 476 and unbiased treatment of the repeating  $T$ -waves, we identify and remove the overlapping noisy  
 477 curvelet coefficients for each given pair in the curvelet denoising.



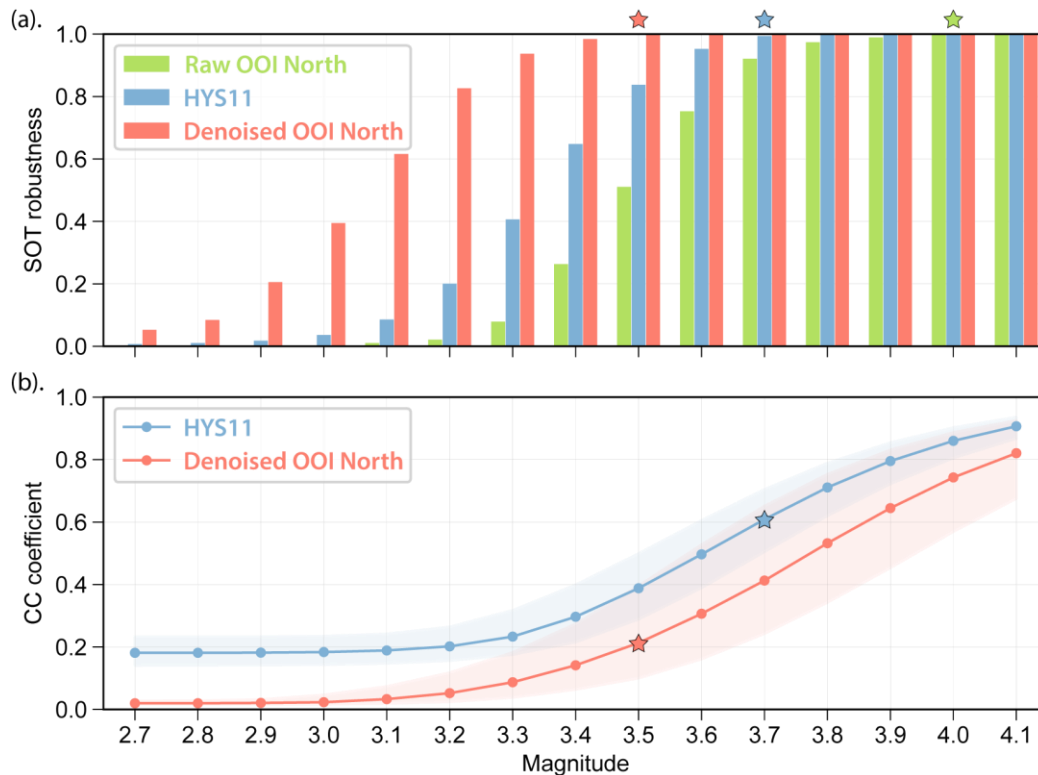
478

479 **Figure 11.** Illustration of improved CCs with curvelet denoising of OBDAS Data. (a). Raw  $T$ -  
 480 wave CCs between two Mw3.5 pseudo-repeating earthquakes at 3-5 Hz. The top panel presents  
 481 the stacked CC (multiplied by 20 for better visualization), the orange shadow area denotes the  
 482 10th-90th percentile of individual CCs. (b). Similar to (a) but for denoised  $T$ -waves.

483 As an example, we generate two M3.5 pseudo-repeating earthquakes by downscaling the  $T$ -waves  
 484 from the Mw5.2 Fox Islands earthquake with a factor of 50. We cut the two repeating  $T$ -waves  
 485 with a 60-s time window and cross correlate them at individual OBDAS channels. However, the  
 486  $T$ -wave signals are so weak relative to the noise that no coherent CC signals are observed (Figure  
 487 11a). The stacked CC waveform exhibits a weak peak at a time shift of -0.27 s, substantially

488 deviating from the input value of 0.0 s. In contrast, curvelet denoising greatly enhances the  $T$ -wave,  
 489 resulting in coherent CC signals that are visible on most channels. The coherent signal is further  
 490 enhanced in the stacked CC waveform with a clear peak amplitude at 0.0 s, matching the expected  
 491 input number (Figure 11b). Here, we first cross correlate individual  $T$ -waves and subsequently  
 492 stack the resulting CCs to accommodate potential waveform variations among different channels.  
 493 Conversely, stacking array waveforms prior to the cross-correlation step may lead to destructive  
 494 interference of  $T$ -waves, compromising the accuracy of the measurements.

495 To ensure robustness, we repeat this M3.5 repeater analysis using all the selected 20 noise windows,  
 496 which yields a total of 190 pseudo-repeating earthquake pairs. We successfully retrieve the  
 497 expected time shift of 0.00 s across all pairs, with an error margin of less than 0.02 s corresponding  
 498 to our downsampled time interval (Figure 12a). Furthermore, we extend the M3.5 scenario to a  
 499 wide range of earthquake magnitude, spanning from M2.7 to M4.1 with an interval of M0.1.  
 500 Curvelet denoising evidently reduces the magnitude required for reliable time shift measurements  
 501 (Figure 12a). Taking a criterion of >99% pairs with successful time shift retrieval (i.e., SOT  
 502 robustness >0.99 in Figure 12a), the magnitude threshold decreases from M4.0 to M3.5. Based on  
 503 the Gutenberg-Richter law (Gutenberg & Richter, 1944), a decrease in magnitude threshold by  
 504 M0.5 would result in a roughly threefold increase in the count of usable repeating events.  
 505 Additionally, the quadratic relationship between the number of repeaters and repeating pairs  
 506 indicates a potential order of magnitude increase of repeating pairs.



508 **Figure 12.** Comparison of SOT performance between OBDAS and OBS. (a). SOT robustness  
 509 using HYS11 data, raw OOI North data, and denoised OOI North data, as a function of earthquake  
 510 magnitude. The SOT robustness is indexed by the ratio of successful pairs, where the input travel  
 511 time shift of 0.00 s is accurately recovered, to the total number of repeating pairs. The stars indicate  
 512 magnitude thresholds, above which >99% pairs accurately retrieve the time shift. (b). CC peak  
 513 amplitudes using HYS11 and denoised OOI North data, as a function of earthquake magnitude.  
 514 The blue represents the median of CC peak amplitudes among the 1400 repeating pairs for HYS11.  
 515 The red line shows the median of stacking CC amplitude peaks among the 190 repeating pairs for  
 516 OOI North. The shadow area indicates the 10th-90th percentiles.

517 We also attempt to evaluate the SOT performance of a neighboring OBS station, specifically  
 518 HYS11, for a comparison with OBDAS (Figure 1). However, during the community experiment,  
 519 HYS11 was inactive for maintenance and did not record the *T*-wave from the M5.2 Fox island  
 520 earthquake. To address the issue, one could involve another M5.2 earthquake recorded by HYS11  
 521 or a different magnitude earthquake with magnitude calibration. However, such an approach can  
 522 introduce substantial uncertainty due to the complex nature of *T*-wave excitation, where even slight  
 523 differences in source parameters can affect *T*-wave amplitudes and thus lead to calibration biases.  
 524 Therefore, we opt not to solely rely on the simplistic calibration method. Alternatively, we leverage  
 525 the NEPTUNE dataset, which captures earthquakes during, after and prior to the experiment, to  
 526 establish a reliable calibration relation between OBDAS and HYS11 (see supplement material text  
 527 S3 for details; Figure S5). Using NEPTUNE as a reference, the calibration method effectively  
 528 cancels out complex effects arising from differences in source parameters and bridges a direct  
 529 comparison between OBS and OBDAS. Similar to the aforementioned evaluation for OBDAS, we  
 530 generate pseudo-repeating pairs for HYS11 by utilizing seven Mw5.0+ Fox islands earthquakes  
 531 (Figure S6) and 200 randomly selected noise waveforms. With a total of 1400 pseudo-repeating  
 532 pairs, the magnitude threshold for HYS11 is M3.7, higher than the threshold of M3.5 for OBDAS  
 533 (Figure 12a). This magnitude difference indicates that using OBDAS can potentially provide four  
 534 times more small repeating pairs for SOT compared to OBS. However, it is important to note that  
 535 our comparison is influenced by the noise level of OBDAS. The current 4-day OBDAS data show  
 536 large variations in noise levels (Figure 8), indicating that long-term OBDAS observations are  
 537 required for a robust quantification. In addition, our estimated magnitude threshold for SOT can  
 538 vary substantially depending on the region and the earthquake source parameters, as *T*-wave  
 539 excitation is strongly modulated by bathymetric features in different regions, resulting in varying  
 540 SNRs of the *T*-wave (de Groot-Hedlin & Orcutt, 2001).

541 In practical SOT applications, a CC coefficient threshold is typically used to ensure accurate *T*-  
 542 wave time shift measurements. Previous studies using *T*-wave stations and hydrophones have  
 543 established an empirical threshold of 0.6 based on visual examination of the CC waveforms,  
 544 lacking a solid justification (Wu et al., 2020). Intriguingly, our pseudo-repeating tests show that  
 545 the median of CC peak amplitudes for HYS11 corresponds to 0.6 at the magnitude threshold of

546 M3.7 (Figure 12b), supporting the previous choices. For OBDAS data, a lower threshold, such as  
547 0.2 for OOI North, can be adopted benefiting from stacking of multiple channels.

## 548 **7 Discussion: Noise in OBDAS data**

549 The noise level in OBDAS data is a critical parameter affecting the *T*-wave data quality. During  
550 the four-day experiment, the OBDAS noise level gradually increased by a factor of 1-2. The source  
551 of OBDAS noise and its temporal variability remain unclear. Analysis of previous OBS data  
552 indicates that tilt and compliance processes are major contributors to OBS noise, both of which  
553 are associated with ocean dynamics (Hilmo & Wilcock, 2020; Janiszewski et al., 2022). While  
554 OBDAS and OBS operate on distinct principles for vibration sensing, their noise sources are not  
555 necessarily identical. Nevertheless, we do observe fluctuations in ocean wave height and wind  
556 direction within the four-day period (Hersbach et al., 2023), suggesting a potential link between  
557 OBDAS noise and ocean dynamics (Figure S7). However, such correlation is still inconclusive  
558 due to limited 4-day data.

559 To evaluate the effect of varying noise on SOT, we randomly select 20 noise samples each from  
560 the first and last 24 hours, representing low and high noise levels, respectively. Consequently, the  
561 magnitude threshold for high-quality SOT increases from M3.2 at low noise level to M3.6 at high  
562 noise level (Figure S8a). Nonetheless, the corresponding median of CC peak amplitudes for both  
563 scenarios consistently fall within the range of 0.1-0.2, reinforcing that a CC coefficient threshold  
564 of 0.2 could be suitable for SOT using a 20-km OBDAS cable regardless of noise level (Figure  
565 S8b). Meanwhile, in previous sections, we use a fixed threshold of 70th percentile noise level for  
566 the stochastic removal. Given the temporal variability of OBDAS noise levels, one may adjust the  
567 threshold for better denoising. Yet, our tests indicate that varying the threshold within the 50th-  
568 100th percentile range barely affects the SOT performance – only the 90th percentile threshold  
569 case marginally outperforms the others (Figure S9). However, our assessment strongly relies on  
570 current dataset and might not be generalized to other OBDAS datasets.

571 Although curvelet denoising efficiently reduces noise, the exact sources of the noise remain  
572 unknown. In particular, the strong incoherent spiky noise is ubiquitous in the OBDAS data (Figure  
573 S10). It often accompanies ocean gravity waves and becomes most pronounced around the peaks  
574 and troughs of these waves (Figure S10). Its amplitude generally increases at shallower water  
575 depths (Figure S10). Intriguingly, higher noise levels in shallower water have also been reported  
576 in OBS data, which are attributed to the seafloor compliance effects due to orbital motions of ocean  
577 waves (Hilmo & Wilcock, 2020; Janiszewski et al., 2022). The spiky noise in OBDAS data also  
578 shows a similar depth dependency, although its exact mechanism remains mysterious. Thus,  
579 further investigations with more data from diverse ocean environments are warranted to better  
580 understand the characteristics and sources of OBDAS noise.

## 581 **8 Conclusions**

582 In this study, we investigate the performance of OBDAS for oceanic seismicity detection and SOT  
583 using the 4-day data collected from the OOI cables offshore central Oregon. To do so, we first  
584 develop a curvelet denoising that effectively enhances *T*-wave signals. This scheme includes  
585 stochastic noise removal, slowness removal and finest-scale removal for different types of noise.  
586 Our results demonstrate that curvelet denoising effectively enhances *T*-wave signal, resulting in a  
587 substantial improvement of *T*-wave event detectability. After denoising, we identify 92 oceanic  
588 events on OOI North, which is three times more than the NEPTUNE catalog. However, the *T*-  
589 wave detectability of OOI North decreases due to a higher noise level during the latter half of the  
590 experiment, highlighting the influences of noise variations. The sensor density and cable  
591 directionality of OBDAS enables us to constrain the source azimuth of regional oceanic seismicity.  
592 We also evaluate the SOT feasibility of OBDAS and juxtapose its performance with conventional  
593 OBSs. To evaluate the feasibility, we synthesize *T*-waves of pseudo-repeating earthquakes using  
594 the observed *T*-waves from a Mw5.2 Fox Islands earthquake and background noise recorded by  
595 OOI OBDAS. Our findings show that OOI OBDAS, leveraging its array data advantage, can  
596 record *T*-waves from a ~3000 km distant repeating earthquake, with a magnitude >M3.5, suitable  
597 for SOT. In contrast, using OBS requires a slightly higher magnitude threshold of M3.7. However,  
598 the performance of OBDAS for oceanic seismicity detection and SOT highly depends on both  
599 natural and instrumental noise levels, which awaits further investigation.

600

## 601 **Acknowledgments**

602 We are grateful for the constructive discussions with Daniel Lizarralde and John A Collins. This  
603 project is supported by the Woods Hole Oceanographic Institution Independent Research &  
604 Development Program. We thank the high-performance computing resources at Woods Hole  
605 Oceanographic Institution made available for conducting this research. Z. S. also acknowledges  
606 the support of the Weston Howland Jr. Postdoctoral Scholarship.

## 607 **Open Research**

608 The curvelet code is available on the curvelet.org website (<http://www.curvelet.org>) and  
609 <https://github.com/atterholt/curvelet-denoising>. The OOI RCA community experiment OBDAS data is available  
610 from <http://piweb.ooirsn.uw.edu/das/>. The ocean wave height and wind speed data are downloaded from  
611 Copernicus Climate Change Service Climate Data Store ([10.24381/cds.adbb2d47](https://doi.org/10.24381/cds.adbb2d47)).

612 **References**

- 613 Allmann, B. P., & Shearer, P. M. (2009). Global variations of stress drop for moderate to large  
614 earthquakes. *Journal of Geophysical Research: Solid Earth*, 114(B1).
- 615 ATOC Consortium. (1998). Ocean climate change: Comparison of acoustic tomography, satellite  
616 altimetry, and modeling. *Science*, 281(5381), 1327-1332.
- 617 Atterholt, J., Zhan, Z., Shen, Z., & Li, Z. (2022). A unified wavefield-partitioning approach for  
618 distributed acoustic sensing. *Geophysical Journal International*, 228(2), 1410-1418.
- 619 Bakun, W. H., & Joyner, W. B. (1984). The ML scale in central California. *Bulletin of the*  
620 *Seismological Society of America*, 74(5), 1827-1843.
- 621 Barnes, C. R., Best, M. M., & Zielinski, A. (2008). The NEPTUNE Canada regional cabled ocean  
622 observatory. *Technology (Crayford, England)*, 50(3).
- 623 Bondár, I., & Storchak, D. A., (2011). Improved location procedures at the International  
624 Seismological Centre. *Geophys. J. Int.*, 186, 1220-1244
- 625 Buehler, J. S., & Shearer, P. M. (2015). T phase observations in global seismogram  
626 stacks. *Geophysical Research Letters*, 42(16), 6607-6613.
- 627 Callies, J., Wu, W., Peng, S., & Zhan, Z. (2023). Vertical-Slice Ocean Tomography With Seismic  
628 Waves. *Geophysical Research Letters*, 50(8), e2023GL102881.
- 629 Candès, E., & Donoho, D. L. (2004). New tight frames of curvelets and optimal representations of  
630 objects with piecewise C2 singularities. *Communications on Pure and Applied Mathematics: A*  
631 *Journal Issued by the Courant Institute of Mathematical Sciences*, 57(2), 219-266.
- 632 Candès, E., Demanet, L., Donoho, D., & Ying, L. (2006). Fast discrete curvelet  
633 transforms. *multiscale modeling & simulation*, 5(3), 861-899.
- 634 Cheng, F., Chi, B., Lindsey, N. J., Dawe, T. C., & Ajo-Franklin, J. B. (2021). Utilizing distributed  
635 acoustic sensing and ocean bottom fiber optic cables for submarine structural  
636 characterization. *Scientific reports*, 11(1), 1-14
- 637 Collins, M.P. (1936). *Bulletin Number 5*. Harvard University Seismograph Station, 23.
- 638 Das, R., Wason, H. R., & Sharma, M. L. (2011). Global regression relations for conversion of  
639 surface wave and body wave magnitudes to moment magnitude. *Natural hazards*, 59, 801-810.
- 640 de Groot-Hedlin, C. D. (2005). Estimation of the rupture length and velocity of the Great Sumatra  
641 earthquake of Dec 26, 2004 using hydroacoustic signals. *Geophysical Research Letters*, 32(11).
- 642 de Groot-Hedlin, C. D., & Orcutt, J. A. (2001). Excitation of T-phases by seafloor scattering. *The*  
643 *Journal of the Acoustical Society of America*, 109(5), 1944-1954.
- 644 Dziak, R. P., Bohnenstiehl, D. R., Matsumoto, H., Fox, C. G., Smith, D. K., Tolstoy, M., ... &  
645 Fowler, M. J. (2004). P-and T-wave detection thresholds, Pn velocity estimate, and detection of  
646 lower mantle and core P-waves on ocean sound-channel hydrophones at the Mid-Atlantic  
647 Ridge. *Bulletin of the Seismological Society of America*, 94(2), 665-677.
- 648 Dziak, R. P., Bohnenstiehl, D. R., & Smith, D. K. (2012). Hydroacoustic monitoring of oceanic  
649 spreading centers: Past, present, and future. *Oceanography*, 25(1), 116-127.

- 650 Fang, J., Yang, Y., Shen, Z., Biondi, E., Wang, X., Williams, E. F., ... & Zhan, Z. (2023).  
651 Directional Sensitivity of DAS and Its Effect on Rayleigh-Wave Tomography: A Case Study in  
652 Oxnard, California. *Seismological Society of America*, 94(2A), 887-897.
- 653 Forget, G. A. E. L., Campin, J. M., Heimbach, P., Hill, C. N., Ponte, R. M., & Wunsch, C. (2015).  
654 ECCO version 4: An integrated framework for non-linear inverse modeling and global ocean state  
655 estimation. *Geoscientific Model Development*, 8(10), 3071-3104.
- 656 Fox, C. G., Dziak, R. P., Matsumoto, H., & Schreiner, A. E. (1993). Potential for monitoring low-  
657 level seismicity on the Juan-de-Fuca ridge using military hydrophone arrays. *Marine Technology*  
658 *Society Journal*, 27(4), 22-30.
- 659 Fox, C. G., Radford, W. E., Dziak, R. P., Lau, T. K., Matsumoto, H., & Schreiner, A. E. (1995).  
660 Acoustic detection of a seafloor spreading episode on the Juan de Fuca Ridge using military  
661 hydrophone arrays. *Geophysical Research Letters*, 22(2), 131-134.
- 662 Fox, C. G., Matsumoto, H., & Lau, T. K. A. (2001). Monitoring Pacific Ocean seismicity from an  
663 autonomous hydrophone array. *Journal of Geophysical Research: Solid Earth*, 106(B3), 4183-  
664 4206.
- 665 Gutenberg, B., & Richter, C. F. (1944). Frequency of earthquakes in California. *Bulletin of the*  
666 *Seismological society of America*, 34(4), 185-188.
- 667 Hamada, N. (1985). T waves recorded by ocean bottom seismographs off the south coast of Tokai  
668 area, central Honshu, Japan. *Journal of Physics of the Earth*, 33(5), 391-410.
- 669 Hanson, J. A., & Bowman, J. R. (2006). Methods for monitoring hydroacoustic events using direct  
670 and reflected T waves in the Indian Ocean. *Journal of Geophysical Research: Solid Earth*, 111(B2)
- 671 Hartog, A. H. (2017). *An introduction to distributed optical fibre sensors*. CRC press.
- 672 Hennenfent, G., & Herrmann, F. J. (2006). Seismic denoising with nonuniformly sampled  
673 curvelets. *Computing in Science & Engineering*, 8(3), 16-25.
- 674 Hersbach, H., Bell, B., Berrisford, P., Biavati, G., Horányi, A., Muñoz Sabater, J., ... & Thépaut,  
675 J. N. (2023). ERA5 hourly data on single levels from 1940 to present. *Copernicus Climate Change*  
676 *Service (C3S) Climate Data Store (CDS)*. 10.24381/cds.adbb2d47 (Accessed on 08-Aug-2023)
- 677 Hilmo, R., & Wilcock, W. S. (2020). Physical sources of high-frequency seismic noise on Cascadia  
678 Initiative ocean bottom seismometers. *Geochemistry, Geophysics, Geosystems*, 21(10),  
679 e2020GC009085.
- 680 Hooft, E. E., Patel, H., Wilcock, W., Becker, K., Butterfield, D., Davis, E., ... & Stakes, D. (2010).  
681 A seismic swarm and regional hydrothermal and hydrologic perturbations: The northern  
682 Endeavour segment, February 2005. *Geochemistry, Geophysics, Geosystems*, 11(12).
- 683 Hyndman, R. D., Riddihough, R. P., & Herzer, R. (1979). The Nootka fault zone—A new plate  
684 boundary off western Canada. *Geophysical Journal International*, 58(3), 667-683.
- 685 Ide, S., Araki, E., & Matsumoto, H. (2021). Very broadband strain-rate measurements along a  
686 submarine fiber-optic cable off Cape Muroto, Nankai subduction zone, Japan. *Earth, Planets and*  
687 *Space*, 73(1), 1-10
- 688 Jaggar, T. A. (1930). How the seismograph works. *The Volcano Letter*, 268, 1-4.

- 689 Janiszewski, H. A., Eilon, Z., Russell, J. B., Brunsvik, B., Gaherty, J. B., Mosher, S. G., ... & Coats,  
690 S. (2023). Broad-band ocean bottom seismometer noise properties. *Geophysical Journal*  
691 *International*, 233(1), 297-315.
- 692 Kelley, D. S., Delaney, J. R., & Juniper, S. K. (2014). Establishing a new era of submarine volcanic  
693 observatories: Cabling Axial Seamount and the Endeavour Segment of the Juan de Fuca  
694 Ridge. *Marine Geology*, 352, 426-450.
- 695 Kennett, B. L. N., & Engdahl, E. R. (1991). Traveltimes for global earthquake location and phase  
696 identification. *Geophysical Journal International*, 105(2), 429-465.
- 697 Komatitsch, D., & Tromp, J. (1999). Introduction to the spectral element method for three-  
698 dimensional seismic wave propagation. *Geophysical journal international*, 139(3), 806-  
699 822. Koyanagi, S., Aki, K., Biswas, N., & Mayeda, K. (1995). Inferred attenuation from site effect-  
700 corrected T phases recorded on the island of Hawaii. *Pure and Applied Geophysics*, 144(1), 1-17.
- 701 Kuna, V. M., Nábělek, J. L., & Braunmiller, J. (2019). Mode of slip and crust–mantle interaction  
702 at oceanic transform faults. *Nature Geoscience*, 12(2), 138-142.
- 703 Li, Z., Shen, Z., Yang, Y., Williams, E., Wang, X., & Zhan, Z. (2021). Rapid response to the 2019  
704 Ridgecrest earthquake with distributed acoustic sensing. *AGU Advances*, 2(2), e2021AV000395.
- 705 Lindsey, N. J., Dawe, T. C., & Ajo-Franklin, J. B. (2019). Illuminating seafloor faults and ocean  
706 dynamics with dark fiber distributed acoustic sensing. *Science*, 366(6469), 1103-1107.
- 707 Lindsey, N. J., & Martin, E. R. (2021). Fiber-optic seismology. *Annual Review of Earth and*  
708 *Planetary Sciences*, 49, 309-336.
- 709 Linehan, D. (1940). Earthquakes in the West Indian region. *Eos, Transactions American*  
710 *Geophysical Union*, 21(2), 229-232.
- 711 Lior, I., Sladen, A., Rivet, D., Ampuero, J. P., Hello, Y., Becerril, C., ... & Markou, C. (2021). On  
712 the detection capabilities of underwater distributed acoustic sensing. *Journal of Geophysical*  
713 *Research: Solid Earth*, 126(3), e2020JB020925.
- 714 Madariaga, R. (1976). Dynamics of an expanding circular fault. *Bulletin of the Seismological*  
715 *Society of America*, 66(3), 639-666.
- 716 Martin, E. R., Lindsey, N. J., Ajo-Franklin, J. B., & Biondi, B. L. (2021). Introduction to  
717 interferometry of fiber-optic strain measurements. *Distributed Acoustic Sensing in Geophysics:*  
718 *Methods and Applications*, 111-129.
- 719 Matsumoto, H., Araki, E., Kimura, T., Fujie, G., Shiraishi, K., Tonegawa, T., ... & Karrenbach, M.  
720 (2021). Detection of hydroacoustic signals on a fiber-optic submarine cable. *Scientific*  
721 *reports*, 11(1), 1-12.
- 722 Matsumoto, H., Haralabus, G., Zampolli, M., & Özel, N. M. (2016). T-phase and tsunami pressure  
723 waveforms recorded by near-source IMS water-column hydrophone triplets during the 2015 Chile  
724 earthquake. *Geophysical Research Letters*, 43(24), 12-511.
- 725 McDougall, T. J., & Barker, P. M. (2011). Getting started with TEOS-10 and the Gibbs Seawater  
726 (GSW) oceanographic toolbox. *Scor/Iapso WG*, 127(532), 1-28.
- 727 Muir, J. B., & Zhan, Z. (2021). Seismic wavefield reconstruction using a pre-conditioned wavelet–  
728 curvelet compressive sensing approach. *Geophysical Journal International*, 227(1), 303-315.

- 729 Munk, W. H., Spindel, R. C., Baggeroer, A., & Birdsall, T. G. (1994). The heard island feasibility  
730 test. *The Journal of the Acoustical Society of America*, 96(4), 2330-2342
- 731 Munk, W., & Wunsch, C. (1979). Ocean acoustic tomography: A scheme for large scale  
732 monitoring. *Deep Sea Research Part A. Oceanographic Research Papers*, 26(2), 123-161
- 733 Okal, E. A. (2001). "Detached" deep earthquakes: are they really? *Physics of the Earth and*  
734 *Planetary Interiors*, 127(1-4), 109-143.
- 735 Okal, E. A. (2008). The generation of T waves by earthquakes. *Advances in Geophysics*, 49, 1-6
- 736 Okal, E. A., & Talandier, J. (1986). T-wave duration, magnitudes and seismic moment of an  
737 earthquake-application to tsunami warning. *Journal of Physics of the Earth*, 34(1), 19-42.
- 738 Parnell-Turner, R., Smith, D. K., & Dziak, R. P. (2022). Hydroacoustic monitoring of seafloor  
739 spreading and transform faulting in the equatorial Atlantic Ocean. *Journal of Geophysical*  
740 *Research: Solid Earth*, 127(7), e2022JB024008.
- 741 Riser, S. C., Freeland, H. J., Roemmich, D., Wijffels, S., Troisi, A., Belbéoch, M., ... & Jayne, S.  
742 R. (2016). Fifteen years of ocean observations with the global Argo array. *Nature Climate*  
743 *Change*, 6(2), 145-153
- 744 Savard, G., Bostock, M. G., Hutchinson, J., Kao, H., Christensen, N. I., & Peacock, S. M. (2020).  
745 The northern terminus of Cascadia subduction. *Journal of Geophysical Research: Solid*  
746 *Earth*, 125(6), e2019JB018453.
- 747 Simon, J. D., Simons, F. J., & Irving, J. C. (2021). A MERMAID miscellany: Seismoacoustic  
748 signals beyond the P wave. *Seismological Society of America*, 92(6), 3657-3667.
- 749 Smith, D. K., Tolstoy, M., Fox, C. G., Bohnenstiehl, D. R., Matsumoto, H., & J. Fowler, M. (2002).  
750 Hydroacoustic monitoring of seismicity at the slow-spreading Mid-Atlantic Ridge. *Geophysical*  
751 *Research Letters*, 29(11), 13-1.
- 752 Sladen, A., Rivet, D., Ampuero, J. P., De Barros, L., Hello, Y., Calbris, G., & Lamare, P. (2019).  
753 Distributed sensing of earthquakes and ocean-solid Earth interactions on seafloor telecom  
754 cables. *Nature communications*, 10(1), 1-8
- 755 Spica, Z. J., Nishida, K., Akuhara, T., Pétrélis, F., Shinohara, M., & Yamada, T. (2020). Marine  
756 sediment characterized by ocean-bottom fiber-optic seismology. *Geophysical Research*  
757 *Letters*, 47(16), e2020GL088360.
- 758 Talandier, J., & Okal, E. A. (2001). Identification criteria for sources of T waves recorded in  
759 French Polynesia. In *Monitoring the Comprehensive Nuclear-Test-Ban Treaty:*  
760 *Hydroacoustics* (pp. 567-603). Birkhäuser, Basel.
- 761 Talandier, J., Hyvernaud, O., Reymond, D., & Okal, E. A. (2006). Hydroacoustic signals generated  
762 by parked and drifting icebergs in the Southern Indian and Pacific Oceans. *Geophysical Journal*  
763 *International*, 165(3), 817-834.
- 764 Talandier, J., & Okal, E. A. (2016). A new source discriminant based on frequency dispersion for  
765 hydroacoustic phases recorded by T-phase stations. *Geophysical Journal International*, 206(3),  
766 1784-1794.
- 767 Tepp, G., & Dziak, R. P. (2021). The seismo-acoustics of submarine volcanic eruptions. *Journal*  
768 *of Geophysical Research: Solid Earth*, 126(4), e2020JB020912.

- 769 Tolstoy, I., & Ewing, M. (1950). The T phase of shallow-focus earthquakes. *Bulletin of the*  
770 *Seismological Society of America*, 40(1), 25-51.
- 771 Tréhu, A. M., Wilcock, W. S., Hilmo, R., Bodin, P., Connolly, J., Roland, E. C., & Braunmiller,  
772 J. (2018). The role of the Ocean Observatories Initiative in monitoring the offshore earthquake  
773 activity of the Cascadia subduction zone. *Oceanography*, 31(1), 104-113.
- 774 Uchida, N., & Bürgmann, R. (2019). Repeating earthquakes. *Annual Review of Earth and*  
775 *Planetary Sciences*, 47(1), 305-332.
- 776 Ugalde, A., Becerril, C., Villaseñor, A., Ranero, C. R., Fernández-Ruiz, M. R., Martin-Lopez, S., ...  
777 & Martins, H. F. (2022). Noise Levels and Signals Observed on Submarine Fibers in the Canary  
778 Islands Using DAS. *Seismological Society of America*, 93(1), 351-363
- 779 Viens, L., Bonilla, L. F., Spica, Z. J., Nishida, K., Yamada, T., & Shinohara, M. (2022). Nonlinear  
780 earthquake response of marine sediments with distributed acoustic sensing. *Geophysical Research*  
781 *Letters*, 49(21), e2022GL100122.
- 782 Walker, D. A., McCreery, C. S., & Hiyoshi, Y. (1992). T-phase spectra, seismic moments, and  
783 tsunamigenesis. *Bulletin of the Seismological Society of America*, 82(3), 1275-1305.
- 784 Webb, S. C. (1998). Broadband seismology and noise under the ocean. *Reviews of*  
785 *Geophysics*, 36(1), 105-142.
- 786 Withers, M., Aster, R., Young, C., Beiriger, J., Harris, M., Moore, S., & Trujillo, J. (1998). A  
787 comparison of select trigger algorithms for automated global seismic phase and event  
788 detection. *Bulletin of the Seismological Society of America*, 88(1), 95-106.
- 789 Wilcock, W. S., Abadi, S., & Lipovsky, B. P. (2023). Distributed acoustic sensing recordings of  
790 low-frequency whale calls and ship noise offshore Central Oregon. *JASA Express Letters*, 3(2),  
791 026002.
- 792 Williams, E. F., Fernández-Ruiz, M. R., Magalhaes, R., Vanthillo, R., Zhan, Z., González-Herráez,  
793 M., & Martins, H. F. (2019). Distributed sensing of microseisms and teleseisms with submarine  
794 dark fibers. *Nature communications*, 10(1), 1-11.
- 795 Williams, E. F., Fernández-Ruiz, M. R., Magalhaes, R., Vanthillo, R., Zhan, Z., González-Herráez,  
796 M., & Martins, H. F. (2021). Scholte wave inversion and passive source imaging with ocean-  
797 bottom DAS. *The Leading Edge*, 40(8), 576-583.
- 798 Williams, E. F., Zhan, Z., Martins, H. F., Fernandez-Ruiz, M. R., Martin-Lopez, S., Gonzalez-  
799 Herraez, M., & Callies, J. (2022). Surface gravity wave interferometry and ocean current  
800 monitoring with ocean-bottom DAS. *Journal of Geophysical Research: Oceans*, e2021JC018375
- 801 Wunsch, C. (2016). Global ocean integrals and means, with trend implications. *Annual Review of*  
802 *Marine Science*, 8, 1-33.
- 803 Wech, A., Tepp, G., Lyons, J., & Haney, M. (2018). Using earthquakes, T waves, and infrasound  
804 to investigate the eruption of Bogoslof volcano, Alaska. *Geophysical Research Letters*, 45(14),  
805 6918-6925.
- 806 Wu, W., Zhan, Z., Peng, S., Ni, S., & Callies, J. (2020). Seismic ocean  
807 thermometry. *Science*, 369(6510), 1510-1515.

- 808 Yu, C., Day, E. A., de Hoop, M. V., Campillo, M., & van der Hilst, R. D. (2017). Mapping mantle  
809 transition zone discontinuities beneath the Central Pacific with array processing of SS  
810 precursors. *Journal of Geophysical Research: Solid Earth*, 122(12), 10-364.
- 811 Zhan, Z. (2020). Distributed acoustic sensing turns fiber-optic cables into sensitive seismic  
812 antennas. *Seismological Research Letters*, 91(1), 1-15.
- 813 Zhang, J., & Langston, C. A. (2020). Separating the scattered wavefield from teleseismic P using  
814 curvelets on the long beach array data set. *Geophysical Journal International*, 220(2), 1112-1127.
- 815 Zhou, Y., Chen, X., Ni, S., Qian, Y., Zhang, Y., Yu, C., ... & Xu, M. (2021). Determining crustal  
816 attenuation with seismic T waves in southern Africa. *Geophysical Research Letters*, 48(15),  
817 e2021GL094410

*Journal of Geophysical Research: Solid Earth*

Supporting Information for

**Ocean bottom distributed acoustic sensing for *T*-wave detection and seismic ocean thermometry**

Zhichao Shen<sup>1</sup> and Wenbo Wu<sup>1</sup>

<sup>1</sup>Department of Geology and Geophysics, Woods Hole Oceanographic Institution, Woods Hole, MA, USA

**Contents of this file**

Text S1 to S6  
Figures S1 to S10  
Tables S1

### **Text S1. Earthquake origin time, location, and magnitude of NEPTUNE *T*-wave catalog**

To determine the origin times and locations of earthquakes in the NEPTUNE *T*-wave catalog, we perform a grid search by minimizing the misfit function  $\psi = \sum_{i=1}^n |t_i^{predict} + t^{origin} - t_i^{pick}|$ , where  $n$  is the number of stations used for grid search. The origin time  $t^{origin}$  is calculated as  $t^{origin} = \frac{1}{n} \sum_{i=1}^n (t_i^{predict} - t_i^{pick})$ , where  $t_i^{predict}$  and  $t_i^{pick}$  denote the predicted and picked seismic arrival time at  $i$ th station, respectively. We use a global 1D model IASP91 to calculate the predicted arrivals (Kennett & Engdahl, 1991). For *P*-waves and *S*-waves, we manually pick up their onset times on the vertical seismograms in a frequency band of 5-10 Hz. The searched area is bounded by 47°N and 52°N in latitude and 126°W and 132°W in longitude with an interval of 0.02°. When *P*-waves and *S*-waves are not available, event locations are constrained by *T*-waves. The arrival times of *T*-waves are picked at their envelop peaks and the searched grids are limited to seismic active areas (Figure S1a).

When clear *P*-waves and *S*-waves are available, we compute the local magnitude given as  $M_L = \log A + \log\left(\frac{D}{100}\right) + 0.00301 * (D - 100) + 3.0$  (Hutton & Boore, 1987), where  $A$  is the peak-to-peak amplitude of Wood Anderson type seismograms and  $D$  represents the epicentral distance. We convert the waveforms to Wood Anderson seismograph, filter them to 2-10 Hz, calculate the peak-to-peak amplitude and then compute the local magnitude by averaging over the three components of all available stations.

### **Text S2. *T*-wave travel time sensitivity kernel**

We use the 2D spectral element method SPECFEM2D (Komatitsch & Tromp, 1999) to compute the *T*-wave travel time sensitivity kernels. Following Wu et al. (2023), we incorporate the global sediment and real bathymetry features to build a 3230 km (distance) X 40 km (depth) 2D slice model. A very shallow sea mountain present on the source-receiver great circle path seriously blocks the *T*-wave propagation, so we take another path, which corresponds to an effective source at 80 km further west, to avoid the strong blocking effects. The ocean sound speeds are calculated using the GSW package (McDougall & Barker, 2011) with the temperature and salinity inputs from the ECCOv4r4 climatology (Forget et al., 2015). The model is meshed with 20,000 (distance) X 96 (depth) elements to resolve 3.5 Hz *T*-wave. We cut the synthetic *T*-wave with a 60 s time window and run adjoint simulations to calculate the *T*-wave travel time sensitivity kernels (Figure S4).

### **Text S3. *T*-wave amplitude ratio between NEPTUNE NCBC and OOI HYS11**

We download the east-component seismograms of the NEPTUNE station NCBC and the OOI station HYS11 for 27 ISC cataloged high-quality *T*-wave events around the Fox islands, bandpass filter the waveforms to 3-5 Hz, calculate the envelopes with a 5-s sliding smooth window, and compute the HYS11/NCBC peak amplitude ratios within a 150-s window after the predicted *T*-wave arrival times (Figure S5). The ISC body wave magnitude  $m_b$  is converted to moment magnitude  $M_w$  using the empirical equation  $M_w = (m_b^{ISC} - 1.65)/0.65$  (Das et al., 2011).

The HYS11/NCBC amplitude ratios have a mean number of 0.35 with a standard deviation of 0.07 (Figure S5). The consistent ratios indicate that *T*-waves at HYS11 and NCBC from earthquakes near the Fox islands share similar propagation effects, that allows us to use NCBC as a reference to synthesize *T*-wave at HYS11 from the Mw5.2 Fox island earthquake. The procedure works as follows: we download the HYS11 east-component seismograms of seven Mw5.3-5.9 earthquakes in this region (Figure S6); For each event, the corresponding *T*-wave is calibrated to Mw5.2 by scaling its own peak amplitude to  $A_{HYS11}^{Mw5.2} = A_{NCBC}^{Mw5.2} * 0.35$ , where  $A_{NCBC}^{Mw5.2}$  is the observed NCBC *T*-wave peak amplitude from the Mw5.2 Fox Island event; Once the Mw5.2 *T*-waves at HYS11 are available, we can follow the same approach as that for the OOI North but use the seven Mw5.2 *T*-waves to conduct the SOT robustness analysis for HYS11 .

#### **Text S4. Correlation between the variations of OBDAS noise level and ocean dynamics**

We download wind significant wave height, wind speed, and wind direction data for the OOI OBDAS region from Copernicus Climate Change Service (C3S) Climate Data Store (CDS; DOI:[10.24381/cds.adbb2d47](https://doi.org/10.24381/cds.adbb2d47)). These parameters are commonly used to characterize the ocean swells and locally generated surface gravity waves. Notably, we observed substantial shifts in the ocean state over the course of the 4-day experiment (Figure S7). In particular, a sudden change in wind direction and significant wave height was recorded on November 4th, 2021, coinciding with the initiation of the increase in OBDAS noise level on the same date.

#### **Text S5. Influence of OBDAS noise level on its performance for SOT**

We randomly select 20 noise samples from the first 24 hours and another 20 noise samples for the last 24 hours, representing low and high noise levels, respectively. We generate 190 pseudo-repeating pairs for each testing earthquake magnitude in each noise level scenario and compute the corresponding SOT robustness and cross-correlation amplitude peaks. It is clear that the high noise level results in deterioration in SOT performance (Figure S8).

#### **Text S6. Testing different noise percentile thresholds for the stochastic removal**

Following the method used in Figure 11a, we randomly select 20 noise windows and generate 190 pseudo-repeating OBDAS pairs for different earthquake magnitudes ranging from M2.7 to M4.1. For each magnitude, we test six different noise thresholds from 50<sup>th</sup> percentile to 100<sup>th</sup> percentile of selected noise for the stochastic removal. After the curvelet denoising, we conduct the SOT measuring for each repeating pair and examine the time shift retrieval. Overall, using the six noise thresholds yields comparable SOT performance, in terms of SOT robustness, across the tested earthquake magnitude range (Figure S9).

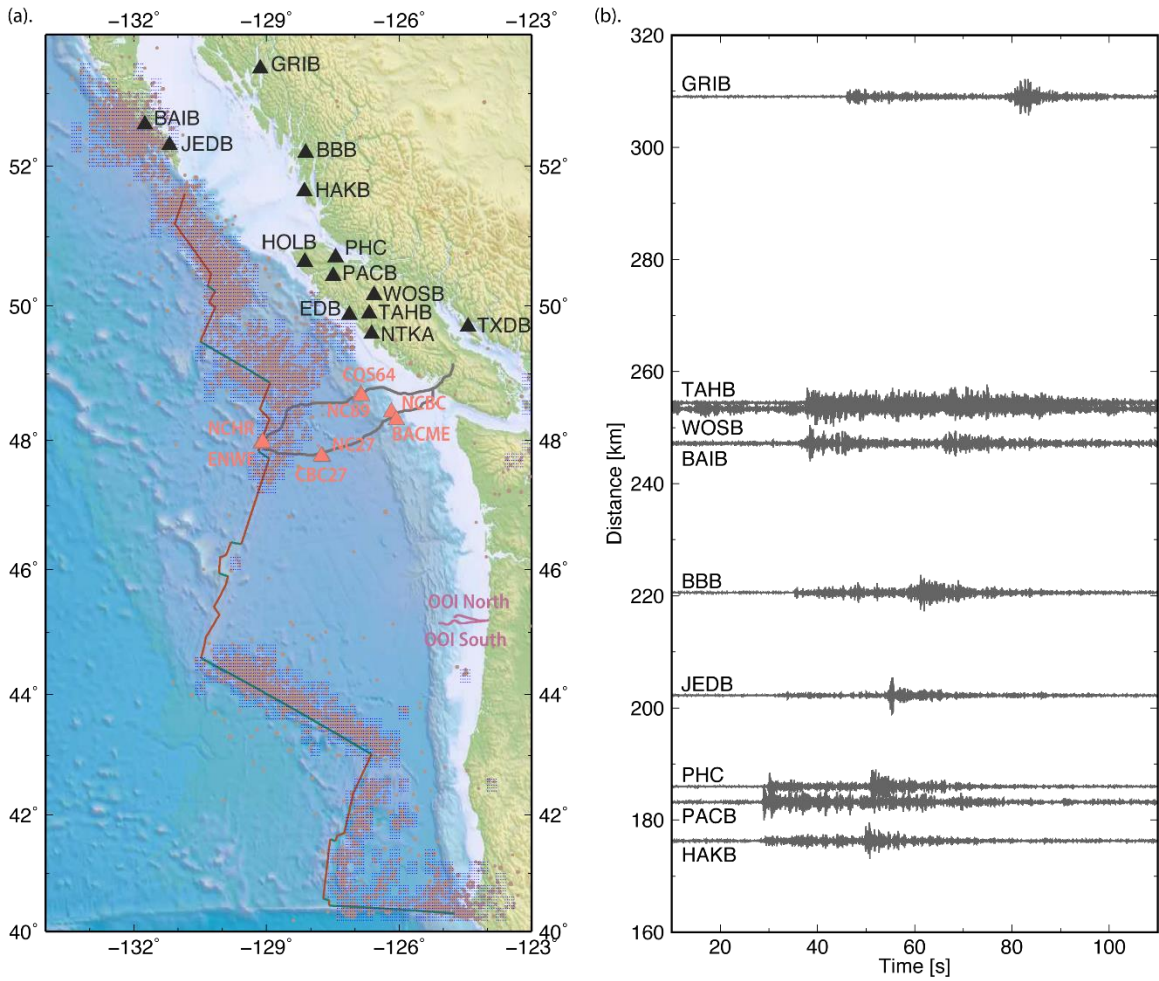


**Figure S1.** (a). Map of background seismicity (dark gray circles), grid-search locations (blue dots) and seismic stations used for locating earthquakes. Black triangles are land stations of which clear *P*-waves and *S*-waves are observed and used for locating earthquakes. (b). An example of *P*-waves and *S*-waves (5-10 Hz) recorded at onshore stations from Event No.11 in Table S1.

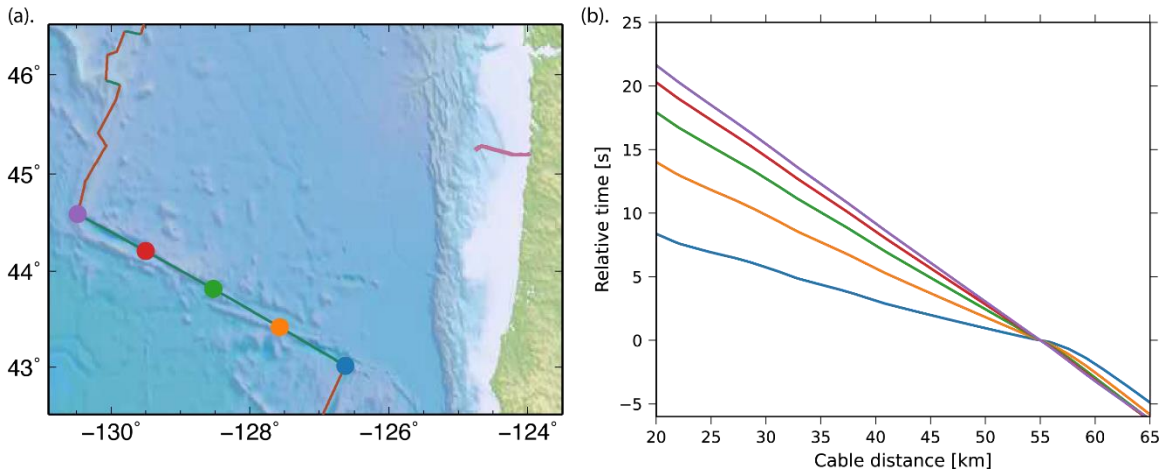


**Figure S2.** OOI North  $T$ -wave slowness sensitivity to earthquake location. (a). Map view of five equally spaced Blanco earthquake testing locations and the OOI North OBDAS. (b). Theoretical  $T$ -wave arrival times on OOI North, relative to that at a cable distance of 55km. Each line shows the arrival times of corresponding testing location in (a). Note the arrival time kinks around 55 km due to a cable geometry change.

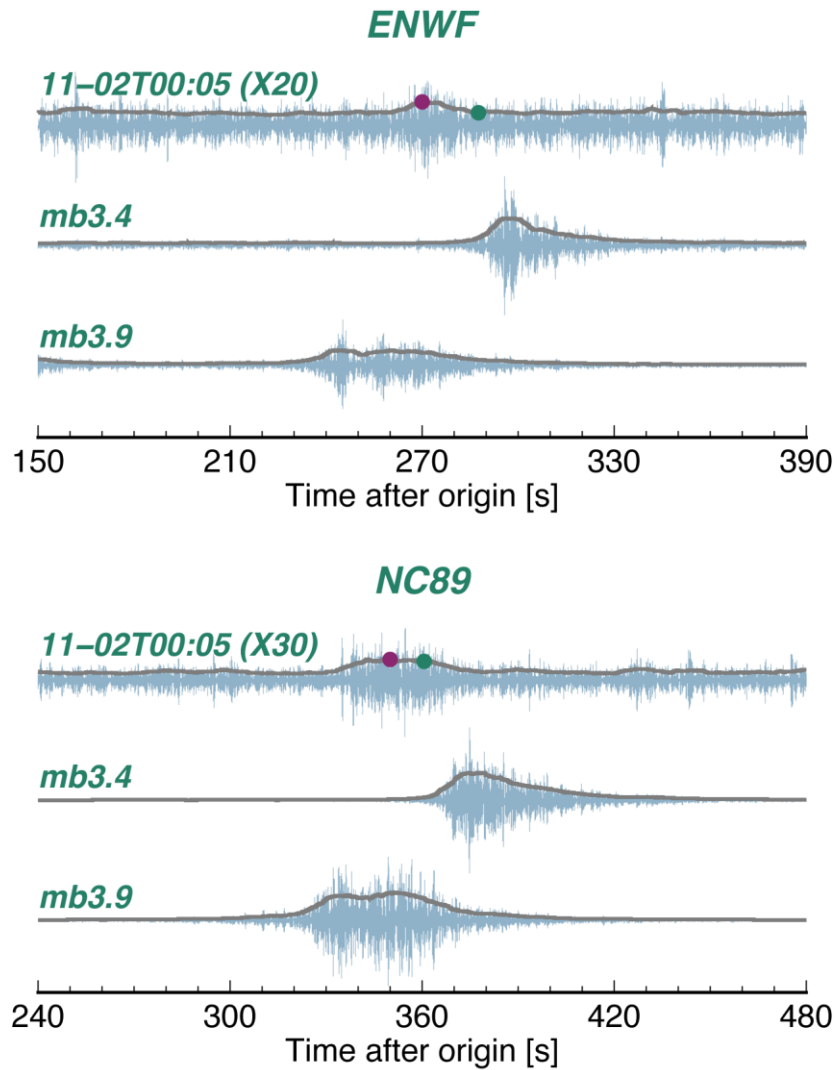


**Figure S3.** *T*-waves observed at two NEPTUNE stations from the 11-02T00:05 Blanco earthquake and two Blanco events (mb3.9 & mb3.4) occurred in 2021-11-01 as shown in Figure 13. The waveforms are bandpass filtered between 4-8 Hz, the gray lines and green dots represent the corresponding envelopes and predicted *T*-wave arrival times from the estimated location of the 11-20T00:05 event in Figure 9, respectively. It is hard to identify *T*-waves at other NEPTUNE stations due to their high noise levels.

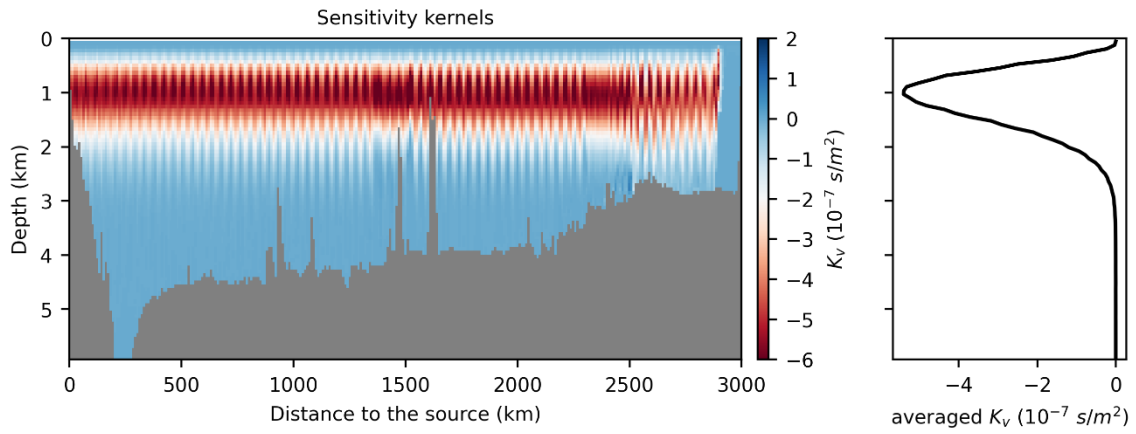


**Figure S4.** *T*-wave travel time sensitivity kernel (2.5-3.5 Hz) for the Aleutian-OOI path. The right panel is the averaged *T*-wave sensitivity kernel along the path.

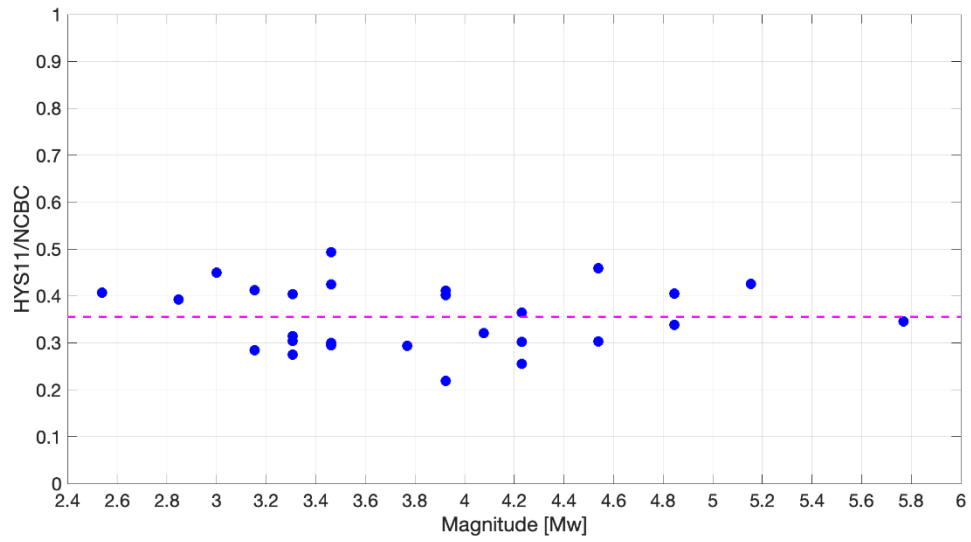


**Figure S5.** Amplitude ratios of *T*-wave envelopes between OOI HYS11 and NEPTUNE NCBC for ISC catalogued earthquakes near the Fox Islands. The dashed line is the averaged ratio (~0.35) among all the data points.

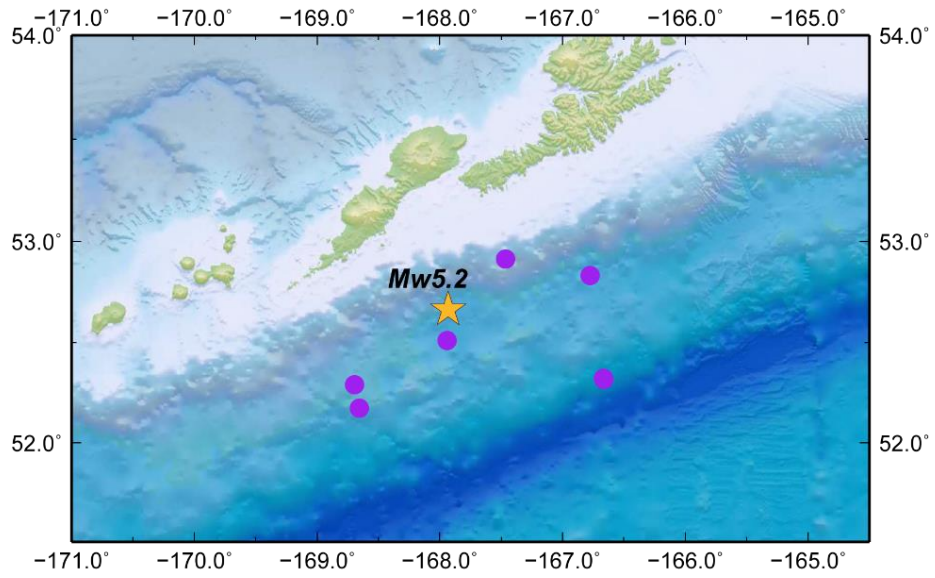


**Figure S6.** Seven moderate size events (purple circles) used in calculating the SOT robustness of HYS11. It is noted that the locations of two events overlap, making them visually hard to distinguish.

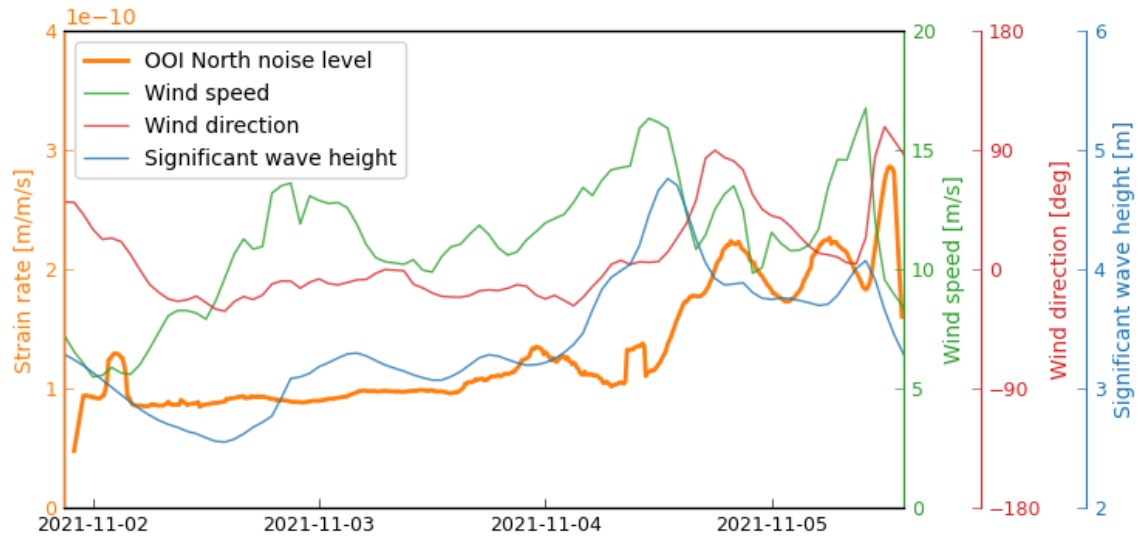


**Figure S7.** Comparison of OBDAS noise level, wind speed (at 10 m above the sea surface), wind direction and significant wave height.

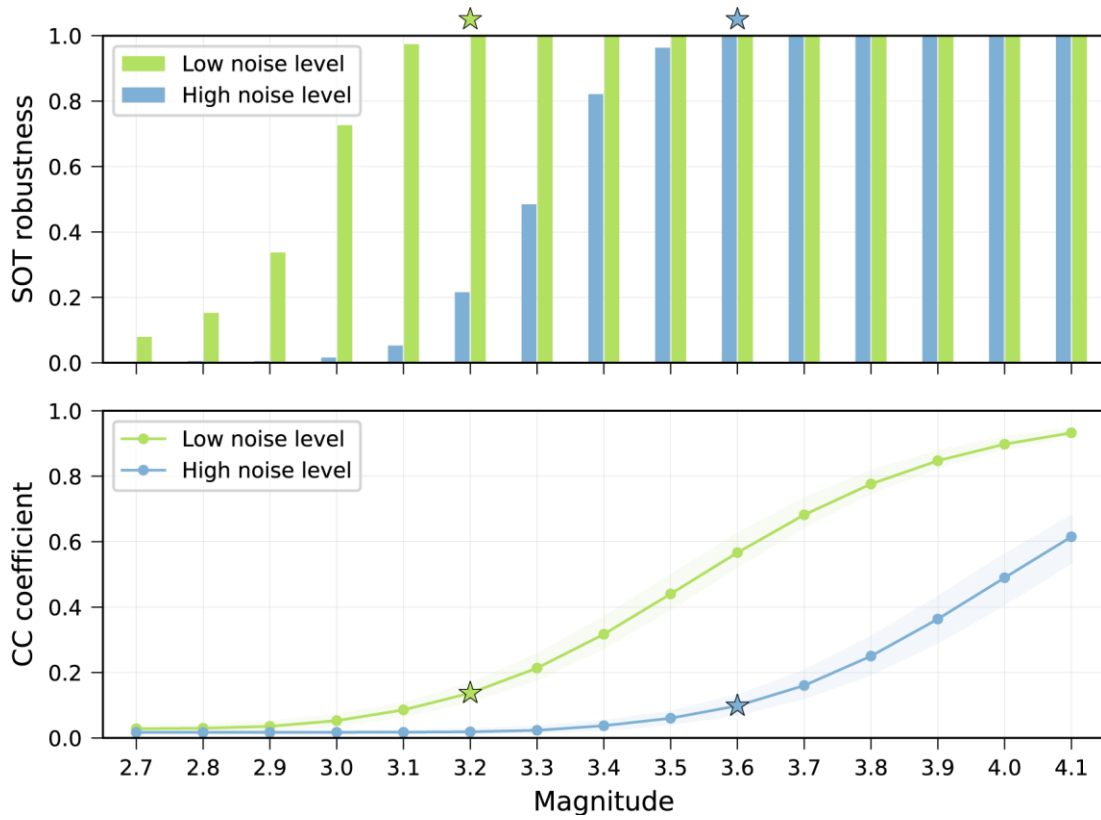


**Figure S8.** Noise effect on OBDAS performance for SOT. (a). Comparison of SOT robustness between low noise level scenario and high noise level scenario for denoised OOI North OBDAS data. (b). Corresponding cross-correlation amplitude between low noise level and high noise level on OBDAS. The stars mark the minimum magnitudes that yield reliable time shift measurements.

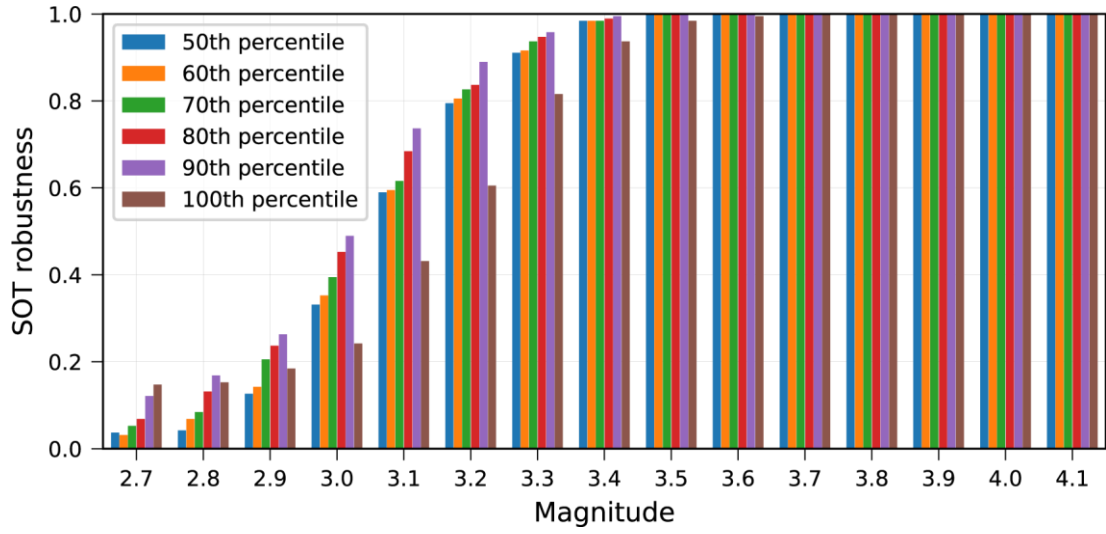


**Figure S9.** Effects of noise threshold in stochastic removal on the OBDAS performance for SOT.

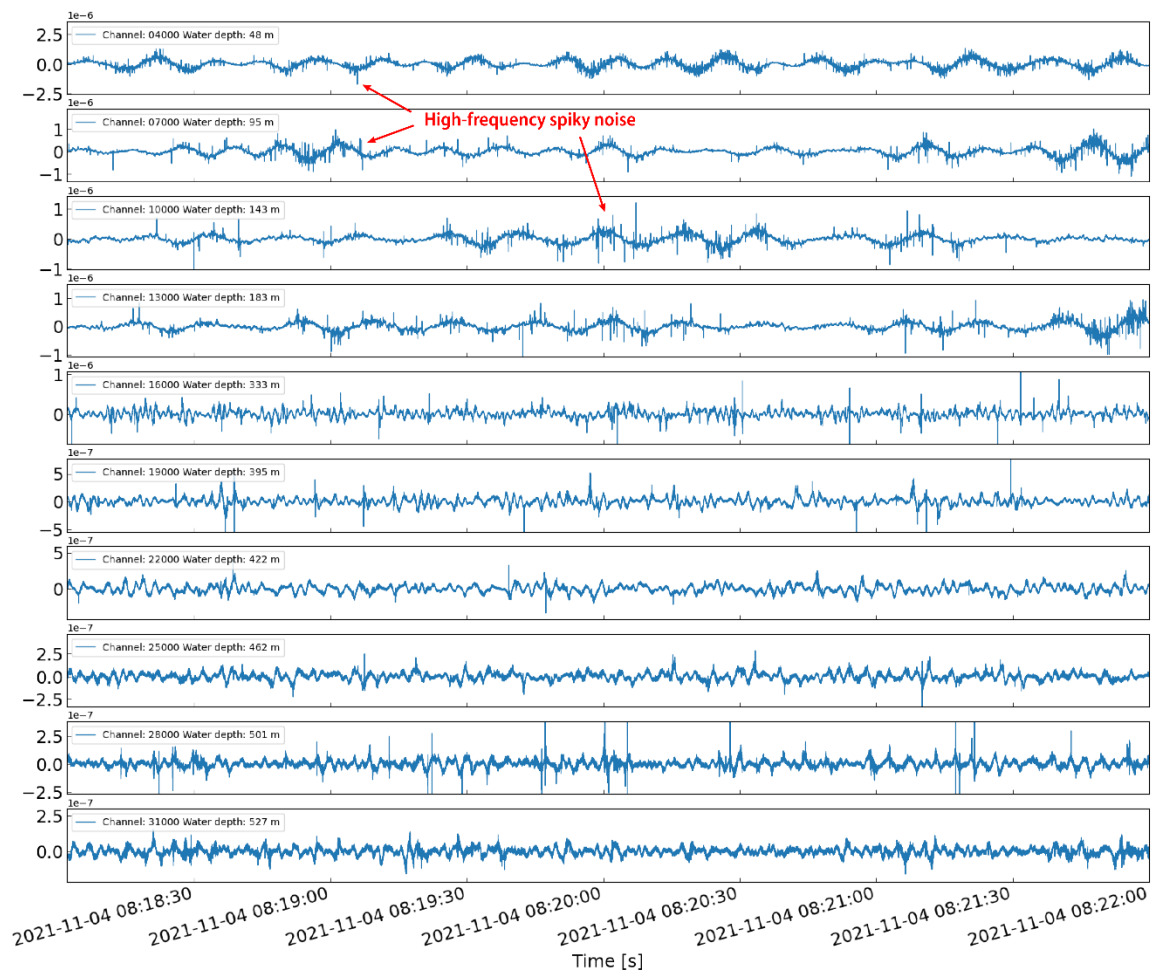


**Figure S10.** 4-min raw strain rate waveforms recorded at OOI North. The channel index is indicated at the top left. Strong high-frequency noises emerge at the peaks and troughs of ocean gravity waves. These noises become weaker in channels at larger ocean depths. Note that the y-axis has a different scale in each subplot.

No.	Event time (UTC)	Latitude	Longitude	Depth [km]	Magnitude	Data used for location
1	2021-11-01 22:59:13.64	47.20°	-129.20°	10.0*	--	<i>T</i> -wave
2	2021-11-01 23:19:59.70	49.16°	-128.32°	10.0*	ML1.6	<i>P</i> -, <i>S</i> -waves
<b>3</b>	<b>2021-11-02 00:11:12.64</b>	<b>43.90°</b>	<b>-129.55°</b>	<b>10.0*</b>	<b>--</b>	<b><i>T</i>-wave</b>
<b>4</b>	<b>2021-11-02 02:14:38.88</b>	<b>50.24°</b>	<b>-129.82°</b>	<b>10.0*</b>	<b>ML2.3</b>	<b><i>P</i>-, <i>S</i>-waves</b>
<b>5</b>	<b>2021-11-02 05:41:35.24</b>	<b>50.40°</b>	<b>-129.78°</b>	<b>10.0*</b>	<b>ML1.7</b>	<b><i>P</i>-, <i>S</i>-waves</b>
<b>6</b>	<b>2021-11-02 08:47:56.82</b>	<b>47.85°</b>	<b>-128.90°</b>	<b>10.0*</b>	<b>--</b>	<b><i>T</i>-wave</b>
<b>7</b>	<b>2021-11-02 12:02:44.29</b>	<b>43.35°</b>	<b>-127.10°</b>	<b>10.0*</b>	<b>--</b>	<b><i>T</i>-wave</b>
8	2021-11-02 13:13:46.84	47.75°	-128.60°	10.0*	--	<i>T</i> -wave
<b>9</b>	<b>2021-11-02 15:01:05.13</b>	<b>47.20°</b>	<b>-129.20°</b>	<b>10.0*</b>	<b>--</b>	<b><i>T</i>-wave</b>
10	2021-11-02 18:01:17.36	49.17°	-128.00°	10.0*	MLSn2.0	ISC catalog
<b>11</b>	<b>2021-11-02 18:15:17.79</b>	<b>50.49°</b>	<b>-130.16°</b>	<b>10.0*</b>	<b>MLSn2.5</b>	<b>ISC catalog</b>
12	2021-11-03 00:24:50.73	40.35°	-124.28°	27.5	Mw4.4	ISC catalog
13	2021-11-03 03:33:51.87	49.08°	-128.06°	10.0*	ML1.8	<i>P</i> -, <i>S</i> -waves
<b>14</b>	<b>2021-11-03 15:43:07.68</b>	<b>47.80°</b>	<b>-129.40°</b>	<b>10.0*</b>	<b>--</b>	<b><i>T</i>-wave</b>
<b>15</b>	<b>2021-11-03 16:20:18.26</b>	<b>47.75°</b>	<b>-128.90°</b>	<b>10.0*</b>	<b>--</b>	<b><i>T</i>-wave</b>
16	2021-11-04 01:59:52.31	47.45°	-128.65°	10.0*	--	<i>T</i> -wave
<b>17</b>	<b>2021-11-04 03:43:21.34</b>	<b>44.20°</b>	<b>-129.05°</b>	<b>10.0*</b>	<b>--</b>	<b><i>T</i>-wave</b>
18	2021-11-04 05:15:01.55	48.65°	-128.35°	10.0*	--	<i>T</i> -wave
<b>19</b>	<b>2021-11-04 05:48:50.15</b>	<b>44.40°</b>	<b>-129.20°</b>	<b>10.0*</b>	<b>--</b>	<b><i>T</i>-wave</b>
<b>20</b>	<b>2021-11-04 08:57:06.93</b>	<b>52.67°</b>	<b>-167.93°</b>	<b>39.3</b>	<b>Mw5.2</b>	<b>ISC catalog</b>

21	2021-11-04 10:23:49.43	47.85°	-128.55°	10.0*	--	<i>T</i> -wave
<b>22</b>	<b>2021-11-04 14:38:35.49</b>	<b>44.70°</b>	<b>-129.05°</b>	<b>10.0*</b>	--	<b><i>T</i>-wave</b>
<b>23</b>	<b>2021-11-04 19:17:15.98</b>	<b>54.73°</b>	<b>-156.92°</b>	<b>10.0</b>	<b>mb4.5</b>	<b>ISC catalog</b>
24	2021-11-04 20:16:14.48	47.20°	-128.80°	10.0*	--	<i>T</i> -wave
<b>25</b>	<b>2021-11-04 20:32:16.45</b>	<b>43.60°</b>	<b>-128.90°</b>	<b>10.0*</b>	--	<b><i>T</i>-wave</b>
<b>26</b>	<b>2021-11-04 23:39:17.62</b>	<b>54.69°</b>	<b>-156.91°</b>	<b>10.0</b>	<b>mb4.0</b>	<b>ISC catalog</b>
<b>27</b>	<b>2021-11-05 05:12:49.48</b>	<b>43.60°</b>	<b>-128.40°</b>	<b>10.0*</b>	--	<b><i>T</i>-wave</b>

**Table S1.** *T*-wave catalog during the OOI DAS experiment using the NEPTUNE array. Symbol \* denotes that the depth is fixed at 10 km. Earthquakes highlighted in red bold font generate identified *T*-waves on OOI DAS.